Durham Research Online

Additional information:

The *NuSTAR* Serendipitous Survey: Hunting for the Most Extreme Obscured AGN at >10 keV

G. B. Lansbury[1,2], D. M. Alexander[2], J. Aird[1], P. Gandhi[3], D. Stern[4], M. Koss[5], I. Lamperti[6], M. Ajello[7], A. Annuar[2], R. J. Assef[8], D. R. Ballantyne[9], M. Baloković[10], F. E. Bauer[11,12,13], W. N. Brandt[14,15,16], M. Brightman[10], C.-T. J. Chen[14], F. Civano[17,18], A. Comastri[19], A. Del Moro[20], C. Fuentes[21], F. A. Harrison[10], S. Marchesi[7], A. Masini[19,22], J. R. Mullaney[23], C. Ricci[11,24], C. Saez[25], J. A. Tomsick[26], E. Treister[11,21], D. J. Walton[1,4,10], and L. Zappacosta[27]

[1] Institute of Astronomy, University of Cambridge, Madingley Road, Cambridge, CB3 0HA, UK; gbl23@ast.cam.ac.uk
[2] Centre for Extragalactic Astronomy, Department of Physics, Durham University, South Road, Durham, DH1 3LE, UK
[3] School of Physics and Astronomy, University of Southampton, Highfield, Southampton SO17 1BJ, UK
[4] Jet Propulsion Laboratory, California Institute of Technology, 4800 Oak Grove Drive, Mail Stop 169-221, Pasadena, CA 91109, USA
[5] Institute for Astronomy, Department of Physics, ETH Zurich, Wolfgang-Pauli-Strasse 27, CH-8093 Zurich, Switzerland
[6] Department of Physics and Astronomy, University College London, Gower Street, London, WC1E 6BT, UK
[7] Department of Physics and Astronomy, Clemson University, Clemson, SC 29634-0978, USA
[8] Núcleo de Astronomía de la Facultad de Ingeniería, Universidad Diego Portales, Av. Ejército Libertador 441, Santiago, Chile
[9] Center for Relativistic Astrophysics, School of Physics, Georgia Institute of Technology, Atlanta, GA 30332, USA
[10] Cahill Center for Astrophysics, 1216 East California Boulevard, California Institute of Technology, Pasadena, CA 91125, USA
[11] Instituto de Astrofísica and Centro de Astroingeniería, Facultad de Física, Pontificia Universidad Católica de Chile, Casilla 306, Santiago 22, Chile
[12] Millennium Institute of Astrophysics, Vicuña Mackenna 4860, 7820436 Macul, Santiago, Chile
[13] Space Science Institute, 4750 Walnut Street, Suite 205, Boulder, CO 80301, USA
[14] Department of Astronomy and Astrophysics, The Pennsylvania State University, University Park, PA 16802, USA
[15] Institute for Gravitation and the Cosmos, The Pennsylvania State University, University Park, PA 16802, USA
[16] Department of Physics, The Pennsylvania State University, University Park, PA 16802, USA
[17] Yale Center for Astronomy and Astrophysics, Physics Department, Yale University, New Haven, CT 06520, USA
[18] Harvard-Smithsonian Center for Astrophysics, 60 Garden Street, Cambridge, MA 02138, USA
[19] INAF-Osservatorio Astronomico di Bologna via Gobetti 93/3 I-40129, Bologna, Italy
[20] Max-Planck-Institut für Extraterrestrische Physik (MPE), Postfach 1312, D-85741, Garching, Germany
[21] Universidad de Concepción, Departamento de Astronomía, Casilla 160-C, Concepción, Chile
[22] Dipartimento di Fisica e Astronomia (DIFA), UniversitÀ di Bologna, viale Berti Pichat 6/2, I-40127 Bologna, Italy
[23] Department of Physics and Astronomy, The University of Sheffield, Hounsfield Road, Sheffield, S3 7RH, UK
[24] Kavli Institute for Astronomy and Astrophysics, Peking University, Beijing 100871, China
[25] Observatorio Astronómico Cerro Calán, Departamento de Astronomía, Universidad de Chile, Casilla 36-D, Santiago, Chile
[26] Space Sciences Laboratory, 7 Gauss Way, University of California, Berkeley, CA 94720-7450, USA
[27] INAF Osservatorio Astronomico di Roma, via Frascati 33, I-00040 Monte Porzio Catone (RM), Italy

Abstract

We identify sources with extremely hard X-ray spectra (i.e., with photon indices of $\Gamma \lesssim 0.6$) in the 13 deg^2 *NuSTAR* serendipitous survey, to search for the most highly obscured active galactic nuclei (AGNs) detected at >10 keV. Eight extreme *NuSTAR* sources are identified, and we use the *NuSTAR* data in combination with lower-energy X-ray observations (from *Chandra*, *Swift* XRT, and *XMM-Newton*) to characterize the broadband (0.5–24 keV) X-ray spectra. We find that all of the extreme sources are highly obscured AGNs, including three robust Compton-thick (CT; $N_{\rm H} > 1.5 \times 10^{24}$ cm^{-2}) AGNs at low redshift ($z < 0.1$) and a likely CT AGN at higher redshift ($z = 0.16$). Most of the extreme sources would not have been identified as highly obscured based on the low-energy (<10 keV) X-ray coverage alone. The multiwavelength properties (e.g., optical spectra and X-ray–mid-IR luminosity ratios) provide further support for the eight sources being significantly obscured. Correcting for absorption, the intrinsic rest-frame 10–40 keV luminosities of the extreme sources cover a broad range, from $\approx 5 \times 10^{42}$ to 10^{45} erg s^{-1}. The estimated number counts of CT AGNs in the *NuSTAR* serendipitous survey are in broad agreement with model expectations based on previous X-ray surveys, except for the lowest redshifts ($z < 0.07$), where we measure a high CT fraction of $f_{\rm CT}^{\rm obs} = 30^{+16}_{-12}\%$. For the small sample of CT AGNs, we find a high fraction of galaxy major mergers ($50\% \pm 33\%$) compared to control samples of "normal" AGNs.

Key words: galaxies: active – galaxies: nuclei – quasars: general – surveys – X-rays: galaxies

1. Introduction

The majority of cosmic supermassive black hole growth has occurred in an obscured phase (e.g., see Brandt & Alexander 2015, for a review), during which gas and dust cover the central active galactic nucleus (AGN). Historically, the importance of highly obscured AGNs has been inferred from the shape of the extragalactic cosmic X-ray background (CXB),

the high-energy hump of which (peaking at ≈ 20–30 keV) requires significant populations of either highly obscured or reflection-dominated systems (e.g., Setti & Woltjer 1989; Comastri et al. 1995; Gilli et al. 2007; Treister et al. 2009). Large population studies have now quantified the relative abundance of obscured and unobscured black hole growth phases (e.g., Aird et al. 2015; Buchner et al. 2015). A

substantial fraction of the growth appears to occur during the most obscured "Compton-thick" (CT) phases, where the absorbing column density exceeds the inverse of the Thomson scattering cross section ($N_H \gtrsim 1.5 \times 10^{24}$ cm^{-2}). However, the intrinsic absorption distribution of AGNs has proven difficult to constrain, especially at the highly obscured to CT end, where AGNs are particularly challenging to identify.

Besides completing a census, identifying the most highly obscured AGNs is crucial to our understanding of the environment of supermassive black hole growth. The unified model of AGNs (e.g., Antonucci 1993; Urry & Padovani 1995; Netzer 2015), which largely succeeds at describing AGNs in the local universe, posits that unobscured, obscured, and CT systems have intrinsically similar nuclear structures but are simply viewed from different inclination angles. In tension with this model (at least in its simplest form) are observational results that find possible evidence for high merger fractions in highly obscured AGN samples (e.g., Kocevski et al. 2015; Del Moro et al. 2016; Koss et al. 2016a; Ricci et al. 2017). Furthermore, observations of the clustering of AGNs find that obscured and unobscured AGNs may inhabit different large-scale environments (e.g., Allevato et al. 2011, 2014; DiPompeo et al. 2014, 2016; Donoso et al. 2014; but see also Mendez et al. 2016; Ballantyne 2017). These results may suggest that high AGN obscuration can be linked to specific phases in the galaxy–AGN coevolutionary sequence (e.g., Sanders et al. 1988; Hopkins et al. 2008; Alexander & Hickox 2012), potentially associated with periods of rapid black hole growth (e.g., Draper & Ballantyne 2010; Treister et al. 2010).

A challenge in answering these questions is that most wavelength regimes are subject to strong biases against detecting highly obscured AGNs, due to a combination of (i) line-of-sight extinction and (ii) dilution by light from other (e.g., stellar) processes. Selection methods exist that are relatively unhindered by (i), such as mid-infrared (MIR) color selection (e.g., Lacy et al. 2004; Stern et al. 2005; Daddi et al. 2007; Fiore et al. 2008; Mateos et al. 2012; Stern et al. 2012) and optical spectroscopic selection based on high-ionization emission lines (e.g., Zakamska et al. 2003; Reyes et al. 2008). However, these techniques both suffer from (ii), especially at sub-quasar luminosities, and both still require X-ray follow-up of the AGNs to provide accurate measurements of the line-of-sight gas column densities (e.g., Vignali et al. 2006; Civano et al. 2007; Alexander et al. 2008; Vignali et al. 2010; Jia et al. 2013; LaMassa et al. 2014; Del Moro et al. 2016). Hard (>10 keV) X-ray observations, on the other hand, have the advantage of very little dilution from other processes and are relatively unaffected by line-of-sight obscuring material up to CT levels of absorption.

For high redshift AGNs ($z \gtrsim 2$) soft X-ray telescopes (e.g., *Chandra* and *XMM-Newton*) sample the rest-frame hard X-ray band and are therefore effective in identifying the features of CT absorption (e.g., Comastri et al. 2011; Brightman et al. 2014). In the lower-redshift universe, however, hard X-ray telescopes become essential. Large (e.g., all-sky) surveys with nonfocusing hard X-ray missions (e.g., *Swift* BAT and *INTEGRAL*) have been important for the identification of highly obscured AGNs in the very local universe ($z < 0.05$; e.g., Burlon et al. 2011; Vasudevan et al. 2013; Ricci et al. 2015; Akylas et al. 2016; Koss et al. 2016a). Now, with the first focusing hard X-ray mission (*NuSTAR*; Harrison et al. 2013) it

is possible to study source populations that are approximately two orders of magnitude fainter, thus extending to lower luminosities and higher redshifts. The largest extragalactic survey being undertaken with *NuSTAR* is the serendipitous survey (Alexander et al. 2013; Lansbury et al. 2017), which has covered ≈13 deg^2 and detected 497 sources, 276 of which have spectroscopic redshifts. The areal coverage and sample size are large compared to the dedicated *NuSTAR* extragalactic blank-field surveys (e.g., in the ECDFS and COSMOS fields; Civano et al. 2015; Mullaney et al. 2015), making the serendipitous survey well suited to the discovery of rare populations such as CT AGNs. The latter have proven elusive in the *NuSTAR* surveys thus far, with only one to two high-confidence CT AGNs being identified overall (e.g., Civano et al. 2015; Del Moro et al. 2017; Zappacosta et al. 2017).

In this paper, we search for the most extreme hard X-ray sources in the 40-month *NuSTAR* serendipitous survey sample, and as a result we reveal new robust CT AGNs. First, we select the objects with the highest *NuSTAR* band ratios, implying very hard spectral shapes and hence the likely presence of heavy absorption. Although band ratios only give a crude estimate of absorption, they are nevertheless an effective way to isolate the most extreme outliers (e.g., Koss et al. 2016a). Second, we perform a detailed analysis of the X-ray and multiwavelength properties of these extreme objects and discuss how their properties compare to those of the general AGN population. The paper is structured as follows. Section 2 describes the selection of the eight extreme objects from the *NuSTAR* serendipitous survey sample. Section 3 details the data used and the soft X-ray counterparts. In Section 4 we characterize the X-ray spectra of the sources (Section 4.1) and present the results for the X-ray spectral properties (Section 4.2). In Section 5 we investigate potential independent estimates of the source obscuration properties through indirect techniques. Section 6 presents the optical properties of the sample, including a summary of the optical spectral properties (Section 6.1) and host galaxy imaging, with a focus on the frequency of galaxy mergers (Section 6.2). In Section 7 we discuss the CT AGNs and their implications for the prevalence of CT absorption within the broader hard-X-ray-selected AGN population. Finally, our main results are summarized in Section 8. The cosmology adopted is $(\Omega_M, \Omega_\Lambda, h) = (0.27, 0.73, 0.70)$. All uncertainties and limits are quoted at the 90% confidence level (CL), unless otherwise stated.

2. The Sample of Extreme, Candidate Highly Obscured AGNs from the *NuSTAR* Serendipitous Survey

We start with the total 40-month *NuSTAR* serendipitous survey sample (497 sources; Lansbury et al. 2017). To select sources with extremely hard X-ray spectra compared to the rest of the *NuSTAR* serendipitous survey sample, we identify sources with high hard-to-soft band ratios (BR$_{Nu}$), calculated as the ratio of the 8–24 keV to 3–8 keV count rates. We apply a cut at BR$_{Nu}$ > 1.7 (see Figure 1), which corresponds to an effective (i.e., observed) photon index of $\Gamma_{eff} \lesssim 0.6$.[28] This cut is motivated by the BR$_{Nu}$ values observed for CT AGNs in other *NuSTAR* programs (e.g., Baloković et al. 2014;

---

[28] The power-law photon index (Γ) is defined as follows: $F_E \propto E^{-\Gamma}$, where F_E is the photon flux and E is the photon energy.
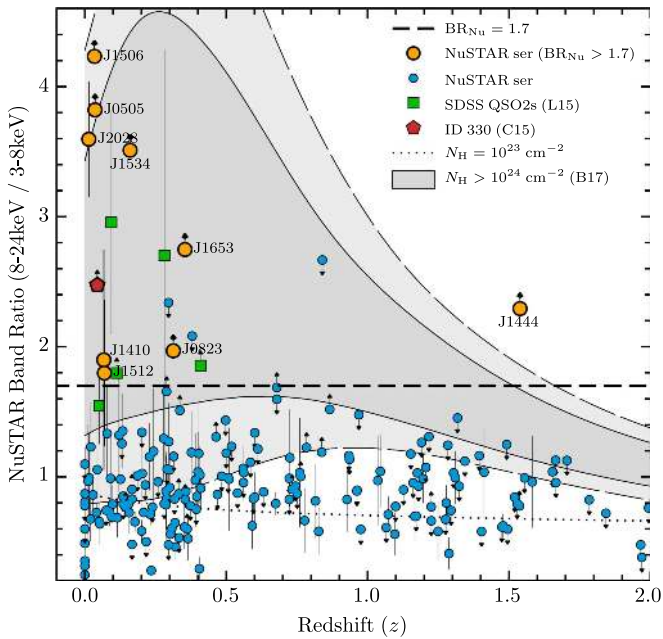
Figure 1. *NuSTAR* band ratio (BR_{Nu}) as a function of redshift (z) for the *NuSTAR* serendipitous survey sample. The extremely hard ($BR_{Nu} > 1.7$; dashed line) serendipitous survey AGNs are shown as orange circles and are individually labeled. "Normal" serendipitous survey sources at $BR_{Nu} < 1.7$ are shown as smaller blue circles. We compare to another extreme sample of optically (SDSS) selected highly obscured Type 2 quasars observed with *NuSTAR* (green squares; Gandhi et al. 2014; Lansbury et al. 2014, 2015), and to ID 330, the CT AGN identified in the *NuSTAR*-COSMOS survey (red pentagon; Civano et al. 2015; Zappacosta et al. 2017). Additionally, we compare to the expected band ratios for CT AGNs based on the high-quality X-ray spectral modeling of very local CT AGNs in the *NuSTAR* snapshot survey (68th percentiles in darker gray with solid borders; 90th percentiles in lighter gray with long-dashed borders; Baloković et al. 2014; M. Baloković et al. 2017, in preparation). For comparison, the dotted black curve shows the band ratios expected for a moderate column density of $N_H = 10^{23}$ cm^{-2}.

Gandhi et al. 2014; Civano et al. 2015; Lansbury et al. 2015). We limit the sample to the sources with spectroscopic redshift measurements and exclude sources with upper limits in BR_{Nu}. The current spectroscopic completeness is ≈70% for the hard-band serendipitous survey sample at high galactic latitudes ($|b| > 10°$; Lansbury et al. 2017).

Figure 1 shows BR_{Nu} versus redshift for the *NuSTAR* serendipitous survey sample, excluding two sources with erroneously high band ratios: NuSTAR J224225+2942.0, for which the photometry is affected by contamination from a nearby bright target, and NuSTAR J172805−1420.9, for which the photometry is unreliable owing to a high surface density of X-ray sources, with multiple *Chandra* sources likely contributing to a blended *NuSTAR* detection (as determined using *Chandra* data obtained through our follow-up program; PI J. A. Tomsick). Overall, nine sources have band ratios exceeding the selection threshold of $BR_{Nu} > 1.7$ (all individually labeled in Figure 1). We exclude NuSTAR J202828+2543.4 (hereafter J2028; $z = 0.01447$) from this work, as the source is closely associated with the science target of the *NuSTAR* field (IGR J20286+2544; projected separation of 26 kpc), and the extreme obscuration and merger properties of this system are the focus of a detailed study in Koss et al. (2016b). The main sample of eight extreme *NuSTAR* sources is listed in Table 1. X-ray images of the sources are shown in Figure 2.

Here we comment on the maximum energies at which the sources are detected with *NuSTAR*. Table 1 lists the standard *NuSTAR* energy bands (i.e., the full, soft, and hard bands) for which sources are detected. By selection, all eight sources are detected in the 8–24 keV band. Splitting this hard band into sub-bands of 8–16 keV and 16–24 keV, all eight sources are detected in the former band, and all except J1444 and J1653 are detected in the latter band. For the six sources detected at 16–24 keV, the highest and lowest Poisson false probabilities are $P_{False} = 2 \times 10^{-3}$ and 10^{-8}, respectively (i.e., the detections range from ≈3σ to highly significant). Only one source shows evidence for emission at >24 keV: J1506, which is detected in the 24–50 keV band at the ≈3σ significance level. In summary, two sources are detected up to a maximum energy of ≈16 keV, five sources are detected up to ≈24 keV, and a single source is weakly detected at even higher energies (up to ≈50 keV).

2.1. A Note on Associated Sources

Six out of eight (75%) of the sources in this sample were serendipitously detected in *NuSTAR* observations of bright low-redshift *Swift* BAT AGNs. The three serendipitous *NuSTAR* sources J0505, J1506, and J1512 are likely to be weakly associated with the brighter BAT AGNs: each source lies within ±500 km s^{-1} of the redshift of the BAT AGN and at a projected separation of ≈150–550 kpc. The associations are "weak" in that the physical separations are large, and the sources are therefore unlikely to be interacting. The associated redshifts are unlikely to occur by chance given that hard X-ray sources at these flux levels ($f_{8-24 keV} = 2$–6×10^{-13} erg s^{-1} cm^{-2}), and within ±500 km s^{-1} of the BAT redshifts, have very low sky densities of ≈0.01 deg^{-2} (e.g., Treister et al. 2009). The latter implies low chance coincidence rates of ≈$10^{-3.5}$ for the three cases of associated redshifts above. The effect of these weak associations on number counts measurements for CT AGNs is accounted for in Section 7.

In the overall 40-month *NuSTAR* serendipitous survey, redshift associations between serendipitous sources and science targets like the above are rare (Lansbury et al. 2017).[29] The exception is at $z < 0.07$, where 10 out of 15 sources (including J0505, J1506, and J1512) show evidence for associations. We emphasize, however, that the majority of extragalactic sources in the *NuSTAR* serendipitous survey (247/262 of the spectroscopically identified sample) are at higher redshifts ($z > 0.07$),[30] meaning that number counts measurements for the survey (e.g., Harrison et al. 2016) are not impacted.

3. Data

Table 2 provides details of the *NuSTAR* and soft (<10 keV) X-ray (i.e., *Chandra*, *Swift* XRT, and *XMM-Newton*) data sets used in this work. For each source we adopt the soft X-ray observatory data that provide the most sensitive coverage at <10 keV. For four sources this coverage is from *Swift* XRT, for three sources it is from *XMM-Newton*, and for one source it is from *Chandra*. For five sources we use the combined soft X-ray data set from multiple individual observations (as

---

[29] Sources are classed as associated if their velocity offset from the science target [$\Delta(cz)$] is smaller than 5% of the total science target velocity (see Lansbury et al. 2017).

[30] At $z > 0.07$ only two sources are flagged as associated.
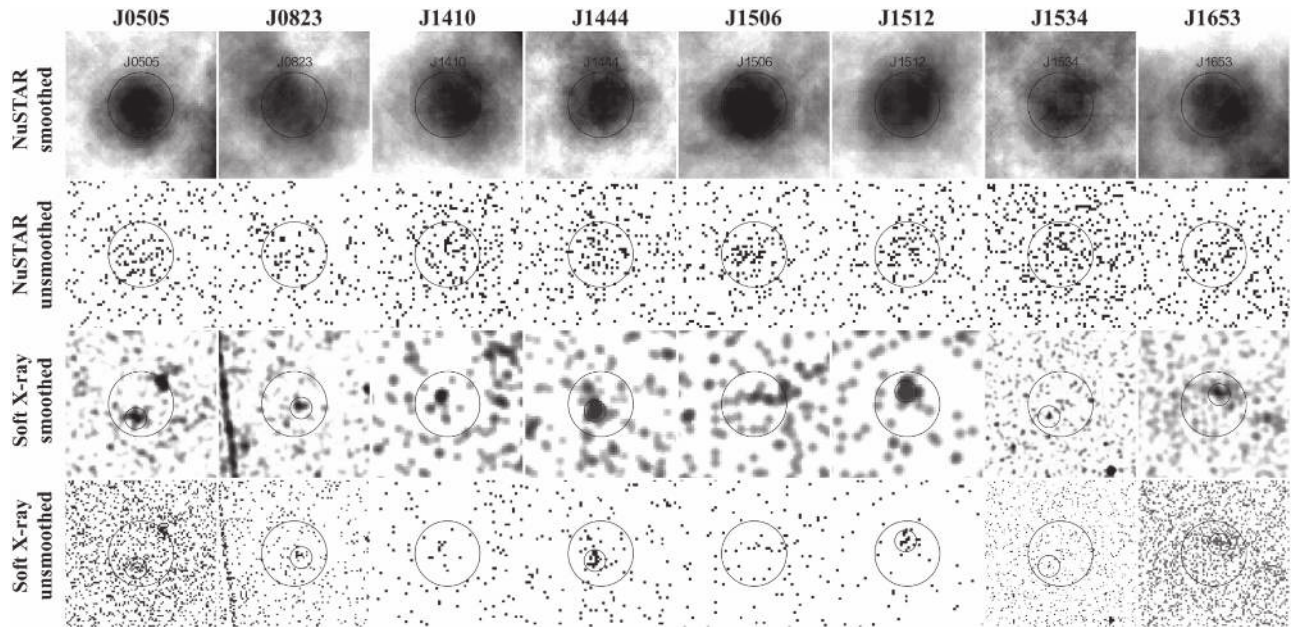
Figure 2. *NuSTAR* and soft X-ray (*Chandra*, *Swift* XRT, and *XMM-Newton*) images for the eight extreme *NuSTAR* serendipitous survey sources. Each column corresponds to an individual *NuSTAR* source (the abbreviated source names are shown). 30″-radius circular apertures are shown for each source, centered on the *NuSTAR* position. Upper two rows: *NuSTAR* hard-band (8–24 keV) images, both smoothed (with a top hat function of radius 14 pixels; first row) and unsmoothed (second row). Lower two rows: soft X-ray images from *Chandra* (the 0.5–2 keV band is shown for J1534), *XMM-Newton* (the full energy band is shown for J0505, J0823, and J1653), and *Swift* XRT (the full energy band is shown for J1410, J1444, J1506, and J1512). The data are shown both smoothed (with a Gaussian function of radius 3 pixels; third row) and unsmoothed (fourth row). The soft X-ray counterpart positions are marked by smaller (10″ radius) circular apertures, for all of the sources except J1410 and J1506 (which are undetected in the available *Swift* XRT coverage; see Section 4).

detailed in Table 2) to obtain the most precise X-ray constraints possible. The soft X-ray observations are generally not contemporaneous with the *NuSTAR* observations. Section 4.1 discusses the possibility of variability for these sources.

3.1. Soft X-Ray Counterparts to the Extreme NuSTAR Sources

The soft X-ray counterparts improve the X-ray positional accuracy and, when combined with the *NuSTAR* data, allow for accurate spectral constraints using the broadest energy band possible. Of the eight extreme *NuSTAR* sources studied here, two lack soft X-ray counterparts (J1410 and J1506). In these cases there is no *Chandra* or *XMM-Newton* coverage, and the sources are undetected in the combined archival *Swift* XRT coverage (running wavdetect with a detection threshold of 10^{-4}). The other six extreme *NuSTAR* sources have identified soft X-ray counterparts. For five of these (J0505, J0823, J1444, J1512, and J1653) the soft X-ray counterparts are identified in Lansbury et al. (2017). Since J0505 has two *XMM-Newton* sources nearby to the *NuSTAR* source, we provide evidence below to support our correct counterpart identification in this case. For the remaining source (J1534), the *Chandra* counterpart is faint and did not satisfy the detection criteria in Lansbury et al. (2017). Below we detail the identification of this specific counterpart.

For J0505, there are two potential counterparts in the 3XMM catalog, one at 14″ offset from the *NuSTAR* position (R.A. = $76°.49983$, decl. = $-23°.83536$; hereafter "XMM1") and one brighter source at 27″ offset (R.A. = $76°.49296$ decl. = $-23°.82597$; hereafter "XMM2"). To examine the X-ray spectra, we use the MOS data for XMM1 (the source lies on a chip gap for PN) and the PN plus MOS data for

XMM2. The 0.5–10 keV spectrum for XMM1 is extremely flat (with an effective photon index of $\Gamma_{\rm eff} = -0.9^{+0.8}_{-1.4}$), and there is a line detection consistent with Fe Kα (rest-frame $E = 6.3 \pm 0.1$ keV). The Fe Kα line has a high equivalent width of $\mathrm{EW_{FeK\alpha}} = 1.4^{+1.4}_{-0.9}$ keV, suggesting a highly absorbed AGN. For XMM2, the 0.5–10 keV spectrum is steeper ($\Gamma_{\rm eff} = 1.4 \pm 0.2$). Although XMM2 is brighter than XMM1 over the full energy band, XMM1 is significantly brighter for the energies at which *NuSTAR* is sensitive: for the 3–10 keV energy band, XMM1 and XMM2 have fluxes of 8.9×10^{-14} erg s^{-1} cm^{-2} and 1.8×10^{-14} erg s^{-1} cm^{-2}, respectively. Given these fluxes and the relative spectral slopes of XMM1 and XMM2 (with the former sharply increasing, and the latter decreasing, toward higher X-ray energies), and the fact that the majority of *NuSTAR* source counts (79%) lie at high energies (>8 keV), we expect XMM1 to dominate the *NuSTAR*-detected emission. We therefore adopt XMM1 as the counterpart to J0505.

For J1534, the deepest soft X-ray coverage is from a 171.5 ks *Chandra* observation (obsID 16092, which targeted Arp 220). Running wavdetect for the broad *Chandra* energy band of 0.5–7 keV, no sources are blindly detected within the *NuSTAR* error circle with false probabilities (i.e., sigthresh values) of $P_{\rm False} \leqslant 10^{-4}$. However, running the source detection for multiple energy bands, there is a significant detection at 0.5–2 keV, with $P_{\rm False} \approx 10^{-6}$. Adding further confidence to the reliability of this source, Sloan Digital Sky Survey (SDSS) coverage reveals a prominent $z = 0.160$ galaxy within the *NuSTAR* error circle (SDSS J153445.80+233121.2), which agrees with the *Chandra* position within the positional uncertainties (0″.6 offset). For an independent assessment of the significance of the *Chandra* source, we perform aperture

Table 1
The Extremely Hard *NuSTAR* Serendipitous Survey Sources

Full Object Name (1)	Short Name (2)	R.A. (3)	Decl. (4)	z (5)	BR_{Nu} (6)	Det. (7)	$N_{H,Gal}$ (8)	Field Name (9)
NuSTAR J050559-2349.9	J0505	76.49839	−23.83169	0.036	>3.8	F H	0.2	2MASX J05054575-235113
NuSTAR J082303-0502.7	J0823	125.76385	−5.04650	0.313	>2.0	F H	0.5	FAIRALL 0272
NuSTAR J141056-4230.0	J1410	212.73727	−42.50139	0.067	1.9 ± 0.8	F S H	0.5	2MASX J14104482-422832
NuSTAR J144406+2506.3	J1444	221.02820	25.10515	1.539	>2.3	F H	0.3	PKS 1441+25
NuSTAR J150645+0346.2	J1506	226.69040	3.77118	0.034	>4.2	F H	0.4	2MASX J15064412+035144
NuSTAR J151253-8124.3	J1512	228.22497	−81.40501	0.069	1.8 ± 0.6	F S H	1.0	2MASX J15144217-812337
NuSTAR J153445+2331.5	J1534	233.68763	23.52593	0.160	>3.5	H	0.4	Arp 220
NuSTAR J165346+3953.7	J1653	253.44313	39.89639	0.354	>2.7	H	0.2	Mrk 501

Note. The sources are listed in order of increasing R.A. The entries in this table are drawn from the *NuSTAR* serendipitous survey source catalog (Lansbury et al. 2017). Column (1): *NuSTAR* serendipitous source name. Column (2): abbreviated *NuSTAR* source name adopted in this paper. Columns (3) and (4): R.A. and decl. J2000 coordinates in decimal degrees. Column (5): source spectroscopic redshift. All redshifts are robust, except for J1444, where fewer lines are identified (see Section 6). Column (6): *NuSTAR* photometric band ratio, as defined in Section 2. Column (7): the *NuSTAR* energy bands for which the source is independently detected. F, S, and H correspond to the full (3–24 keV), soft (3–8 keV), and hard (8–24 keV) bands, respectively. Column (8): line-of-sight Galactic column density (Kalberla et al. 2005). Units: 10^{21} cm^{-2}. Column (9): name of the *NuSTAR* science target, in the field of which the serendipitous source is detected.

photometry (2″ source radius; large background annulus) at the SDSS position. For the 0.5–2 keV band, the source is indeed detected at the 4.0σ level (according to the binomial false probability). The *NuSTAR*/*Chandra* flux ratio for J1534 is extremely high (e.g., $f_{8-24}/f_{0.5-2} = 141$). For comparison, four sources in the *NuSTAR*-COSMOS survey have similarly high flux ratios (ranging from $f_{8-24}/f_{0.5-2} = 100$ to 304), and all of these have been identified as highly obscured AGNs (e.g., Brightman et al. 2014; Lanzuisi et al. 2015; Zappacosta et al., 2017). The *Chandra* spectrum for J1534 is further discussed in Section 4.1.

3.2. X-Ray Spectroscopic Products

The NuSTARDAS task `nuproducts` is used to extract *NuSTAR* source spectra, background spectra, and response files.[31] We adopt circular source extraction regions of 45″ radius where possible, and of 30″ radius for two cases where the source is either close to a bright science target or to the field-of-view (FOV) edge. We perform separate spectral extractions for the two individual *NuSTAR* telescopes (FPMA and FPMB). For J0823, we limit the modeling to FPMB, since the source is only fully within the *NuSTAR* FOV for FPMB.

For the six sources with soft X-ray counterparts, we extract additional spectra from the archival soft X-ray data sets detailed in Table 2, using the relevant software packages (the *Chandra* Interactive Analysis Observations software,[32] the *Swift* XRT analysis software distributed with HEASoft,[33] and the *XMM-Newton* Science Analysis Software[34]). We adopt source extraction apertures of 5″, 10″, and 12″–15″ radius for the *Chandra*, *Swift* XRT, and *XMM-Newton* data, respectively. For J1444 we co-add the *Swift* XRT spectra across all six observations, since the source is only significantly detected in the co-added data.

4. X-Ray Properties

4.1. X-Ray Spectral Modeling

We perform X-ray spectral modeling using XSPEC (version 12.8.1j; Arnaud 1996) with the *C*-statistic (`cstat`) setting,[35] which is more appropriate than χ^2 in the low-counts regime (e.g., Nousek & Shue 1989). We group the data (source plus background) from *NuSTAR* and from other X-ray missions by a minimum of 3 counts and 1 count per bin, respectively, as recommended for use with `cstat`.[36]

In all cases, we fit a simple unabsorbed power-law model in order to constrain the effective photon index (Γ_{eff}) and thus obtain a basic measure of the overall X-ray spectral slope. Figure 3 shows the *NuSTAR* plus soft X-ray (*Chandra*, *Swift* XRT, or *XMM-Newton*) spectra for the eight extreme *NuSTAR* serendipitous survey sources, with power-law model fits to each. Flat Γ_{eff} values (e.g., $\lesssim 0.5$) give empirical evidence for high or CT absorption. Further empirical evidence for CT absorption can be obtained from the detection of a strong fluorescent Fe Kα emission line at ≈ 6.4 keV (with an equivalent width of $EW_{Fe K\alpha} > 1$ keV, although lower values do not necessarily rule out CT absorption; e.g., Della Ceca et al. 2008; Gandhi et al. 2017). This reflection feature becomes more prominent with increasing levels of absorption (e.g., Risaliti 2002). To place constraints on $EW_{Fe K\alpha}$ for our sources, we model the rest-frame ≈ 4–9 keV spectrum as a power law (to fit the continuum) plus an unresolved Gaussian at rest-frame $E = 6.4$ keV. For two sources (J0505 and J1512) the emission line is well detected, and $EW_{Fe K\alpha}$ is therefore constrained. For the remaining six sources the line is undetected, due to insufficient counts, and we report upper limits on $EW_{Fe K\alpha}$ (assuming a line width of $\sigma_{line} = 0.1$ keV) where the data allow informative constraints. In Table 3 we provide the basic observed X-ray spectral properties for the sample: effective photon indices, Fe Kα line equivalent widths, and observed (i.e., uncorrected for absorption) X-ray luminosities.

---

[31] http://heasarc.gsfc.nasa.gov/docs/nustar/analysis
[32] Fruscione et al. (2006); http://cxc.harvard.edu/ciao/index.htm
[33] http://www.swift.ac.uk/analysis/xrt/
[34] http://xmm.esa.int/sas/

[35] The *W* statistic is actually used, since the background is unmodeled; see http://heasarc.gsfc.nasa.gov/docs/xanadu/xspec/wstat.ps..
[36] https://asd.gsfc.nasa.gov/XSPECwiki/low_count_spectra

Table 2
Summary of the X-Ray Data Adopted for the Spectroscopic and Photometric X-Ray Analyses

	NuSTAR Observations					Soft X-ray Observations					
Object (1)	Observation ID (2)	UT Date (3)	t (4)	S_{net} (5)	B (6)	Observatory (7)	Observation ID (8)	UT Date (9)	t (10)	S_{net} (11)	B (12)
J0505	60061056002	2013 Aug 21	21.1	66	53	*XMM-Newton*	0605090101[c]	2009 Aug 06	29.4	70	46
J0823	60061080002[a]	2014 Jan 10	24.3	41	67	*XMM-Newton*	0501210501	2007 Oct 14	8.4	12	9
J1410	60160571002	2015 May 14	22:2	153	125	*Swift* XRT	00040973002	2010 Sep 27	5.0	⋯	⋯
							00040973003	2011 Mar 10	5.0	⋯	⋯
							00081157002	2015 Apr 30	5.8	⋯	⋯
							00081157003	2015 May 14	5.6	⋯	⋯
J1444	90101004002	2015 Apr 25	38.2	62	153	*Swift* XRT	⋯	⋯	19.6[d]	10	⋯
							00033768001	2015 May 13	3.1	⋯	⋯
							00033768002	2015 May 18	3.0	⋯	⋯
							00033768003	2015 Jun 01	4.1	⋯	⋯
							00033768004	2015 Sep 04	4.0	⋯	⋯
							00033768005	2016 Apr 13	4.0	⋯	⋯
							00033768006	2016 Apr 17	1.4	⋯	⋯
J1506	60061261002	2014 Sep 08	21.3	81	122	*Swift* XRT	00036622001	2007 Dec 19	9.4	⋯	⋯
							00036622002	2007 Dec 21	8.7	⋯	⋯
							00080144001	2014 Sep 08	6.1	⋯	⋯
J1512	60061263002	2013 Aug 06	13.3	153	74	*Swift* XRT	00036623001	2007 Jun 07	6.2	11	⋯
							00036623002	2007 Jun 09	5.3	7	⋯
							00080146001	2013 Aug 06	6.8	11	⋯
J1534	60002026002[b]	2013 Aug 13	66.7	42	133	*Chandra*	16092	2014 Apr 30	171.5	10	10
J1653	60002024002[b]	2013 Apr 13	18.3	14	16	*XMM-Newton*	0652570101[c]	2010 Sep 08	43.7	73	47
							0652570201[c]	2010 Sep 10	44.0	82	42

Notes. Column (1): abbreviated *NuSTAR* source name. Columns (2) and (3): *NuSTAR* observation ID and start date (YYYY MM DD). Columns (4), (5), and (6): net exposure time (ks), net source counts, and scaled background counts, respectively, for the extracted 3–24 keV (or 8–24 keV for J1534 and J1653) *NuSTAR* spectrum. Column (7): soft X-ray observatory with the best (or in some cases, the only) coverage, which we adopt for the analyses. Columns (8) and (9): adopted soft X-ray observation ID(s) and their corresponding start date(s) (YYYY MM DD), respectively. Columns (10), (11), and (12): exposure time (ks), net source counts, and scaled background counts, respectively. For J0505, J0823, J1444, J1512, J1534, and J1653, these columns correspond to the extracted X-ray spectra (at 0.5–10 keV, 0.6–10 keV, and 0.5–8 keV for *XMM-Newton*, *Swift* XRT, and *Chandra*, respectively). For the remaining two sources that are undetected at soft X-ray energies (1410 and J1506), the *Swift* XRT data tabulated here are used for photometric constraints.
[a] Here we use the *NuSTAR* FPMB data only (i.e., excluding the FPMA data).
[b] In these cases we limit the *NuSTAR* spectral analysis to the 8–24 keV band, since the sources are undetected in the soft (3–8 keV) and full (3–24 keV) *NuSTAR* bands, indicating no significant source emission at <8 keV.
[c] In these cases we use the combined MOS1+MOS2 data only.
[d] Here we quote the total exposure time and counts (summing across all observations), since the source is undetected in individual *Swift* XRT observations.

We use three more spectral models in order to constrain the source properties such as the intrinsic absorbing column density (N_H), the intrinsic photon index (Γ), and the X-ray luminosity. First, we fit a transmission-only model (hereafter the `transmission` model): a power law attenuated by redshifted photoelectric absorption and Compton scattering of photons out of the line of sight (CABS · ZWABS · POW, in XSPEC formalism). This model represents one extreme of obscured AGN spectra, where the X-ray spectrum is dominated by the primary AGN continuum transmitted directly along the line of sight. Second, we fit a reflection-only model (hereafter the `reflection` model), which represents a power-law spectrum reflected by circumnuclear material. For this we use the PEXRAV model (Magdziarz & Zdziarski 1995), with the reflection scaling factor set to −1 to yield a pure reflection spectrum, and with the other parameters set to default values. This model represents the other extreme of obscured AGN spectra, where the X-ray spectrum is dominated by the reflected AGN continuum, which (in combination with strong Fe line emission) implies very high column densities ($N_H \gg 10^{24}$ cm^{-2}). At high column densities, X-ray spectra are typically more complex than the `transmission` and `reflection` models above, and ideally any absorbed continuum, reflected continuum, and fluorescent line emission should be modeled in a self-consistent way and assuming a well-motivated geometry. We therefore perform an additional third test using the BNTORUS model (hereafter the `torus` model; Brightman & Nandra 2011), which was produced using simulations of X-ray radiative transfer through a toroidal distribution of gas. We set the model to an edge-on torus configuration (with $\theta_{inclination}$ and θ_{torus} set to 87° and 60°, respectively). In this form, the `torus` model has the same number of free parameters as the `transmission` and `reflection` models and is therefore no less suited to the statistical quality of the data. For every model fit, we account for Galactic absorption with a PHABS multiplicative component, fixed to column density values from Kalberla et al. (2005). In cases where Γ and N_H cannot be simultaneously constrained, we fix the intrinsic photon index at $\Gamma = 1.9$ (a typical value for AGNs detected at 3–24 keV; e.g., Alexander et al. 2013; Del Moro et al. 2017). In Table 4 we show the best-fit parameters obtained by applying the three models described above: intrinsic photon indices, column densities, fit statistics, and intrinsic (i.e., absorption-corrected) luminosities.
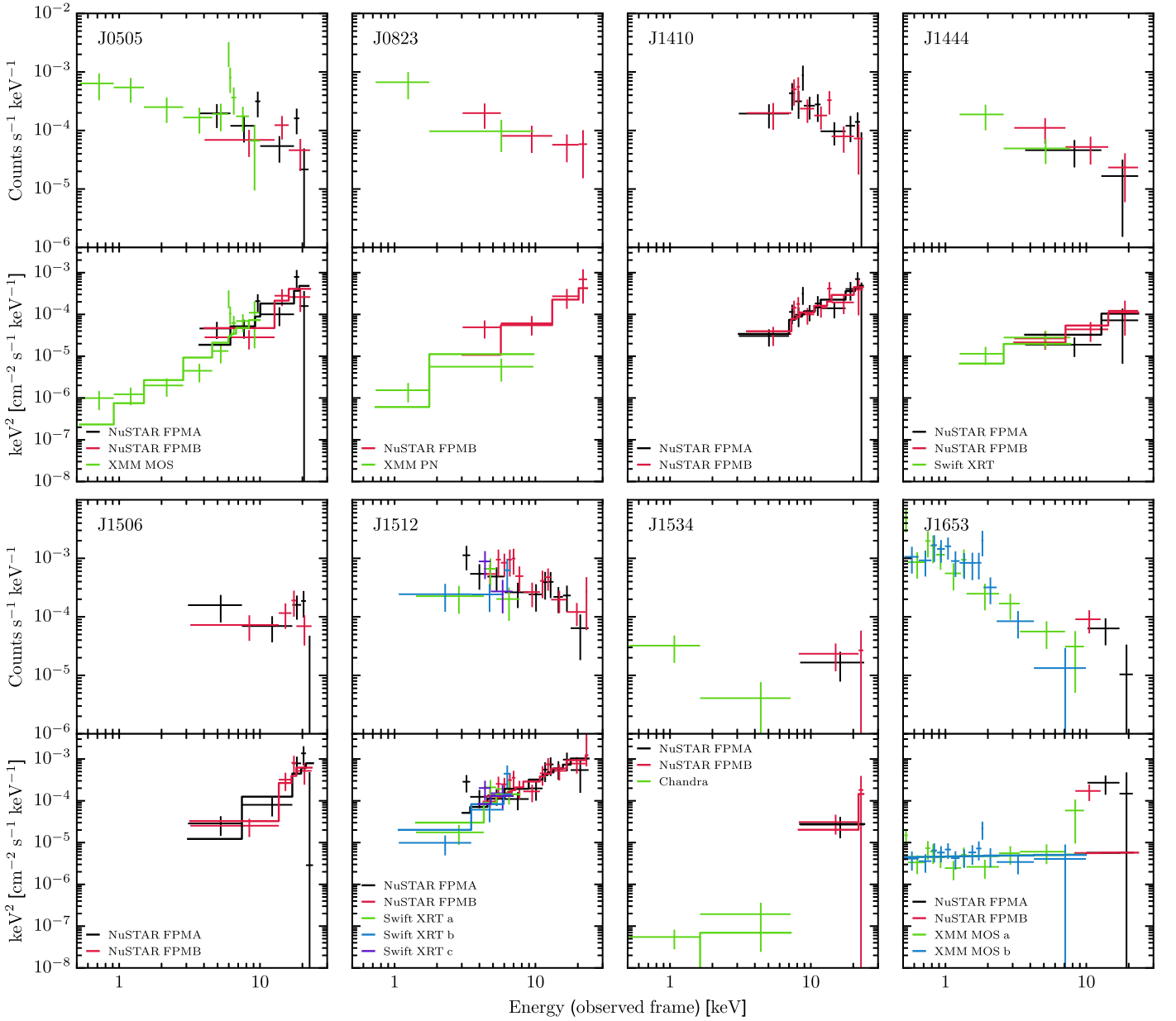
Figure 3. X-ray spectra in observed count-rate units (top panel for a given source) and in EF_E units (bottom panel for a given source) for the eight extreme *NuSTAR* sources (Section 4). Black and red correspond to *NuSTAR* FPMA and FPMB, respectively. The green, blue, and purple spectra represent the available soft X-ray data (as labeled). Letter suffixes (e.g., *Swift* XRT b) indicate separate observations. See Table 2 for a full description of the adopted data sets. The data are binned to a minimum significance of 2σ per bin for visual purposes. The EF_E spectra are shown with best-fitting power-law models, binned to match the data (solid lines).

In one case (J1653) we find that an additional soft-X-ray-dominated model component is necessary to obtain an acceptable fit to the data. For J1653 all three models provide a poor fit to the *XMM-Newton* plus *NuSTAR* spectrum (for the transmission, reflection, and torus models, the ratio of the C statistic to the number of degrees of freedom is $C/n = 352/200$, $311/202$, and $335/201$, respectively) and leave strong positive residuals at high energies ($\gtrsim 8$ keV). This is due to an apparently sudden change in the spectral shape, with the low energies ($\lesssim 4$ keV) dominated by a steep ($\Gamma \approx 2$) component and the higher energies ($\gtrsim 4$ keV) dominated by a flatter component ($\Gamma \approx -0.5$). One way to interpret this is an electron-scattered or leaked (due to partial covering) AGN power law at lower energies and a primary AGN continuum

penetrating through at higher energies, as is commonly observed for well-studied AGNs in the local universe (e.g., Cappi et al. 2006). The relatively high luminosity ($L_{0.5-4\,\mathrm{keV}} \approx 7 \times 10^{42}\,\mathrm{erg\,s^{-1}}$) justifies the scattered AGN power-law interpretation rather than, e.g., thermal emission associated with star formation. For J1653 we therefore add an unobscured power-law component to the three spectral models, with the spectral slope tied to that of the intrinsic AGN power-law continuum. This results in statistically improved fits (see the C/n values in Table 4) and reasonable scattered power-law fraction constraints ($f_{\mathrm{scatt}} \approx 0.04\% - 5\%$).

The source J1534 also shows evidence for a steep soft component in the *Chandra* spectrum ($\Gamma_{\mathrm{eff}} \approx 3$ at 0.5–8 keV), which is dominated by photon counts at <2 keV (as described

Table 3
Basic X-Ray Spectral Parameters

Object (1)	$\Gamma_{\rm eff}^{\rm NuSTAR}$ (2)	$\Gamma_{\rm eff}^{\rm soft}$ (3)	$EW_{\rm FeK\alpha}$ (4)	$L_{2-10}^{\rm obs}$ (5)	$L_{10-40}^{\rm obs}$ (6)
J0505	$-0.1^{+0.7}_{-0.8}$	$-0.9^{+0.8}_{-1.4}$	$1.4^{+1.4}_{-0.9}$	41.3	42.3
J0823	$0.3^{+1.1}_{-1.3}$	$1.2^{+1.2}_{-0.9}$	...	42.5	44.4
J1410	0.3 ± 0.4	...	<1.7	42.0	42.7
J1444	$-0.3^{+0.9}_{-1.2}$	0.7 ± 1.1	<1.4	44.7	45.1
J1506	$-0.7^{+0.9}_{-1.6}$	...	<3.2	39.9	42.6
J1512	$0.9^{+0.4}_{-0.5}$	$-0.6^{+0.7}_{-0.9}$	$0.76^{+1.04}_{-0.56}$	42.4	43.2
J1534	$<-0.9^{\rm a}$	$3.3^{+5.9}_{-2.4}$	...	39.8	42.7
J1653	$-0.5^{+0.9{\rm a}}_{-0.6}$	2.0 ± 0.3	<0.5	42.7	44.3

Note. Column (1): abbreviated *NuSTAR* source name. Column (2): *NuSTAR* effective photon index, i.e., the photon index obtained from approximating the *NuSTAR* 3–24 keV spectrum as a simple power law. For the sources marked. Column (3): "soft" effective photon index, measured using the available soft X-ray spectra from *Chandra*, *Swift* XRT, or *XMM-Newton* (over the full energy range for the relevant observatory; ≈0.5–10 keV). Column (4): constraint on the Fe Kα line equivalent width. Units: keV. Columns (5) and (6): logarithm of the observed (i.e., uncorrected for absorption) X-ray luminosities in the rest-frame 2–10 keV and 10–40 keV bands, respectively. Units: erg s^{-1}.
[a] The constraint was obtained using a combination of *NuSTAR* and soft X-ray (*XMM-Newton* or *Swift* XRT) data, due to weak *NuSTAR*-only constraints.

in Section 3.1). This is uncharacteristic of pure AGN emission and indicates that at low X-ray energies there is a significant contribution to the spectrum from other radiative processes in the host galaxy. We find that the detection of this soft component is due to the primary AGN spectrum being highly absorbed (see Sections 4.2 and 5) so as not to be well detected by *Chandra*. Indeed, the AGN is only detectable at >8 keV with *NuSTAR*. The luminosity of the soft X-ray emission ($L_{2-10}^{\rm obs} = 10^{39.8}$ erg s^{-1}; Table 3) is in broad agreement with the expectations for normal galaxy emission based on the X-ray main sequence of star formation (Aird et al. 2017) and given the stellar mass of J1534 ($M_\star = 10^{11.1} M_\odot$; based on the spectral energy distribution (SED) modeling in Section 5). If the soft component is instead interpreted as a scattered AGN power law, then the scattered fraction must be small ($f_{\rm scatt} \lesssim 0.05\%$). For the spectral modeling of J1534 below, we parameterize the steep soft emission with an additional power-law component. We also tested a different approach of simply excluding the <2 keV photons, and this yields consistent values for the intrinsic source properties.

For the sources where we model the *NuSTAR* data simultaneously with soft X-ray (*Chandra*, *Swift* XRT, or *XMM-Newton*) data, there is a general caveat that the soft X-ray observations are not contemporaneous with the *NuSTAR* data, and AGN variability could thus affect the interpretations. Although highly obscured AGNs such as those presented here show some evidence for lower variability compared to unobscured AGNs (e.g., Awaki et al. 2006), significant variability on year-long timescales is still possible (e.g., Yang et al. 2016; Masini et al. 2017). While our sources generally show no evidence for significant variability (e.g., see the overlapping data in Figure 3), the spectral uncertainties are generally too large to rule out low-level (e.g., factors of $\lesssim 2$) variability. We thus fix the cross-normalization constants to standard values: 1.0 for *Chandra*:*NuSTAR*, 1.0 for *Swift* XRT: *NuSTAR*, and 0.93 for *XMM-Newton*:*NuSTAR* (e.g., Madsen

et al. 2015). There is one exception, J0823, where the *XMM-Newton*:*NuSTAR* cross-normalization parameter must be left free to obtain statistically acceptable solutions. The `transmission` and `torus` models converge to extremely low cross-normalization constants (≈0.01), and we therefore limit the modeling to the *NuSTAR* data only. The best-fit `reflection` model, however, has a less extreme cross-normalization constant of $0.12^{+0.19}_{-0.08}$ when fitting the *XMM-Newton* plus *NuSTAR* data set. The low cross-normalization constants for J0823 may be due to X-ray variability between the 2007 *XMM-Newton* and the 2014 *NuSTAR* observations, although we do not draw strong conclusions given the uncertainties for this source.

4.2. Results for the X-Ray Source Properties

Here we summarize the measured X-ray properties. Figure 4 shows the effective photon indices (i.e., the observed spectral slopes) of the sources, as measured with individual X-ray observatories, as a function of X-ray luminosity (uncorrected for absorption). The extreme *NuSTAR* sources cover a broad range in luminosity. The *NuSTAR*-measured effective photon indices (right panel of Figure 4) are generally very low (median value of $\Gamma_{\rm eff} = -0.2$ at 3–24 keV), giving empirical evidence for very high absorption levels. We compare against another sample of extreme systems: highly obscured SDSS-selected Type 2 quasars targeted with *NuSTAR* (Gandhi et al. 2014; Lansbury et al. 2014, 2015). The two extreme samples cover a similar range of spectral slopes and lie at significantly harder values (i.e., lower $\Gamma_{\rm eff}$ values) than the general population of "normal" *NuSTAR* serendipitous survey sources (also shown in Figure 4, for sources with constrained $\Gamma_{\rm eff}$ values; Lansbury et al. 2017). The measured spectral slopes show a large scatter at soft energies (≈0.5–10 keV; using *Chandra*, *Swift* XRT, and *XMM-Newton*). For the *NuSTAR*-observed SDSS Type 2 quasars, this scatter was found to be partly due to an increased contamination at these lower X-ray energies from radiative processes other than the direct AGN emission (e.g., Lansbury et al. 2015), which may also be the case for some of the extreme *NuSTAR* sources (namely, J1534 and J1653; see Section 4.1). In other words, soft X-ray observations alone would fail to identify $57^{+19}_{-21}\%$ of the extreme sources in Figure 4 as highly obscured using spectral slope information (assuming a threshold of $\Gamma_{\rm eff} = 1$). *NuSTAR* observations, on the other hand, are highly reliable at identifying the most highly obscured AGNs.

For the purposes of comparing $N_{\rm H}$ constraints and estimating intrinsic luminosities ($L_{\rm X}$; shown in Table 4), we adopt the `torus` model solutions. In one exception (J0823) we adopt the lower-$N_{\rm H}$ `transmission` model solution. The adopted best-fitting $N_{\rm H}$ and $L_{\rm X}$ values are shown in Figure 5. Based on these intrinsic luminosity constraints, the more distant AGNs ($z > 0.2$) are at "X-ray quasar" luminosities ($L_{\rm X} \gtrsim 10^{44}$ erg s^{-1}), and the less distant AGNs ($z < 0.2$) range from relatively low luminosities up to the quasar threshold ($L_{\rm X} \approx 10^{42.7}$–$10^{44}$ erg s^{-1}). The $N_{\rm H}$ constraints shown may be conservative for sources where the `reflection` model gives a statistically acceptable fit to the X-ray spectrum (indicating consistency with $N_{\rm H} \gg 10^{24}$ cm^{-2}). For a similar reason, the Compton-thin constraints shown for J1410 and J1444 may be conservative; the `torus` modeling also finds statistically acceptable reflection-dominated model solutions at very high CT column densities ($N_{\rm H} > 6 \times 10^{24}$ cm^{-2}) in these cases.

**Table 4**
Best-fit Parameters for the X-Ray Spectral Modeling

Object	E Range (keV)	pow $\Gamma_{\rm eff}$	C/n	transmission Γ	$N_{\rm H}$ (10^{24} cm^{-2})	C/n	reflection Γ	C/n	torus Γ	$N_{\rm H}$ (10^{24} cm^{-2})	C/n	$L^{\rm int}_{2-10}$	$L^{\rm int}_{10-40}$	CT
(1)	(2)	(3)	(4)	(5)	(6)	(7)	(8)	(9)	(10)	(11)	(12)	(13)	(14)	(15)
J0505	0.5–24	-0.2 ± 0.2	164/142	[1.9]	$0.87^{+0.37}_{-0.27}$	159/139	1.3 ± 0.4	148/139	$2.5^{+0.4}_{-0.8}$	$1.5^{+4.7}_{-0.5}$	148/142	43.1	42.7	Y
J0823	0.5–24	-0.2 ± 0.7	78/54	[1.9]	$0.73^{+1.51}_{-0.61}$	45/33[a]	$2.6^{+1.0}_{-0.7}$	71/53	[1.9]	$12.6^{+u}_{-12.0}$	41/33[a]	44.4	44.4	⋯
J1410	3–24	0.3 ± 0.4	78/87	[1.9]	$0.74^{+0.31}_{-0.25}$	78/87	1.8 ± 0.4	82/87	[1.9]	$0.63^{+0.31}_{-0.24}$[b]	80/87	⋯	43.0	⋯
J1444	0.6–24	0.8 ± 0.5	98/75	[1.9]	$0.21^{+0.28}_{-0.17}$	104/75	$2.1^{+0.7}_{-0.6}$	102/75	[1.9]	$0.21^{+0.28}_{-0.17}$[b]	103/75	45.1	45.1	⋯
J1506	3–24	$-0.7^{+0.9}_{-1.6}$	77/64	[1.9]	$5.0^{+3.6}_{-3.7}$	82/64	[1.9]	79/65	$1.5^{+1.2}_{-u}$	$4.1^{+u}_{-2.3}$	70/63	⋯	43.3	Y
J1512	0.6–24	0.4 ± 0.2	123/98	[1.9]	$0.13^{+0.22}_{-0.06}$	142/98	$2.1^{+0.2}_{-0.3}$	112/98	$2.8^{+u}_{-0.8}$[c]	$2.9^{+u}_{-1.2}$	112/97	44.6	44.0	Y
J1534	0.5–24	$-2.3^{+1.5}_{-u}$	90/74	[1.9]	$2.5^{+u}_{-1.2}$	84/72	[1.9]	90/73	[1.9]	$1.6^{+u}_{-1.1}$	87/72	42.7	42.7	y
J1653	0.5–24	$1.9^{+0.4}_{-0.3}$	182/194	$2.3^{+0.5}_{-0.4}$	$2.4^{+1.3}_{-0.9}$	165/192	$2.4^{+0.8}_{-0.5}$	179/193	$2.3^{+0.6}_{-0.5}$	$1.6^{+1.5}_{-1.1}$	175/192	44.3	44.1	y?

Notes. Column (1): abbreviated *NuSTAR* source name. Column (2): energy range modeled (units of keV). Columns (3) and (4): best-fit results for the unobscured power-law model (pow; also shown in Figure 3), where $\Gamma_{\rm eff}$ is the power-law photon index. Columns (5)–(12): best-fit results for the transmission, reflection, and torus models, respectively. These include the intrinsic photon index (Γ; square brackets indicate fixed values), the column density ($N_{\rm H}$; units of 10^{24} cm^{-2}), and the fit statistic (C/n, where C is the C-statistic and n is the number of degrees of freedom). An error value of $+u$ or $-u$ indicates that the parameter is unconstrained at the upper or lower end. Columns (13) and (14): logarithm of the intrinsic (i.e., absorption-corrected) X-ray luminosities in the rest-frame 2–10 keV and 10–40 keV bands, respectively. Units: erg s^{-1}. Column (15): flag to indicate high-confidence CT AGNs and likely CT AGNs (marked as "Y" and "y," respectively). J1653 is marked as "y?" since there is multiwavelength evidence against a CT interpretation (Section 5). For the three sources marked as "⋯" we cannot strongly rule out CT absorption based on the X-ray modeling.

[a] As detailed in Section 4.1, the transmission and torus model fits for J0823 are performed for the *NuSTAR* data only (i.e., the *XMM-Newton* data are excluded).

[b] For two sources (J1410 and J1444) we show the conservative low-$N_{\rm H}$ torus model solution in this table, but in each case there is also a second similarly valid solution at very high column densities (for J1410, $N_{\rm H} > 6 \times 10^{24}$ cm^{-2} and $C/n = 92/87$; and for J1444, $N_{\rm H} > 6 \times 10^{24}$ cm^{-2} and $C/n = 102/75$).

[c] For J1512, fixing Γ to more typical values results in even higher $N_{\rm H}$ solutions (e.g., a lower limit of $N_{\rm H} > 8 \times 10^{24}$ cm^{-2} for $\Gamma = 1.9$).
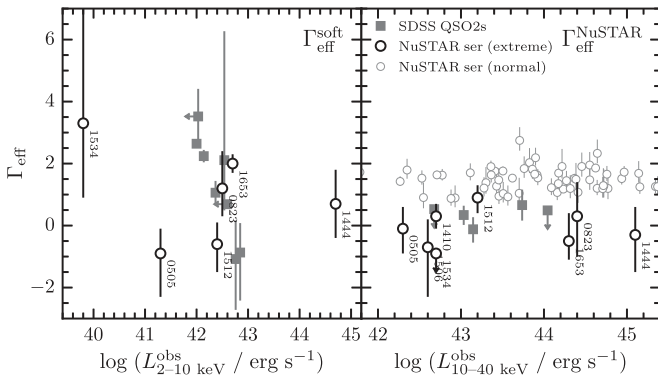
Figure 4. Observed X-ray properties: effective photon index (i.e., spectral slope) vs. rest-frame X-ray luminosity (uncorrected for absorption). The left panel shows the properties measured at soft X-ray energies (with *Chandra*, *Swift* XRT, or *XMM-Newton*), and the right panel shows the properties measured at harder X-ray energies with *NuSTAR*. $\Gamma_{\rm eff}^{\rm soft}$ and $\Gamma_{\rm eff}^{\rm NuSTAR}$ are measured for the observed-frame $\approx$0.5–10 keV and 3–24 keV bands, respectively. We compare the extreme *NuSTAR* serendipitous survey sources (black circles, individually labeled) to "normal" serendipitous survey sources (smaller gray circles) and to highly obscured and CT Type 2 quasars which were optically selected and followed up with *NuSTAR* observations (filled gray squares; Gandhi et al. 2014; Lansbury et al. 2014, 2015).
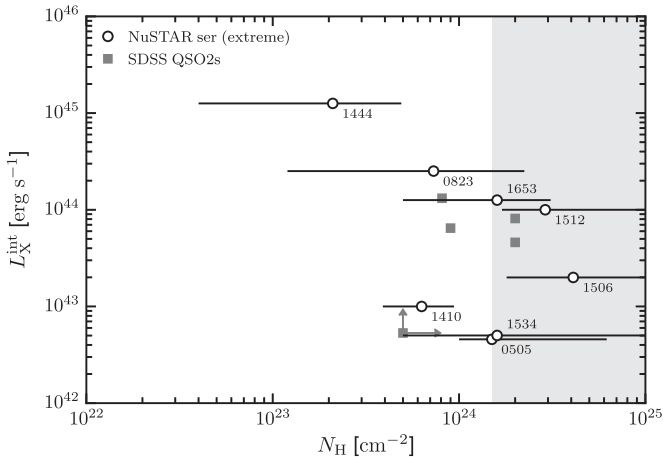
Figure 5. Rest-frame intrinsic (i.e., absorption-corrected) 10–40 keV X-ray luminosity (L_X) vs. column density (N_H), from modeling the X-ray spectra of the extreme *NuSTAR* serendipitous survey sources (open circles). Each data point corresponds to the `torus` model solution (except J0823, where the `transmission` model solution is shown). Following Figure 4, the filled gray squares show a comparison sample of highly obscured Type 2 quasars (Gandhi et al. 2014; Lansbury et al. 2014, 2015). The CT column density region ($N_H \geqslant 1.5 \times 10^{24}$ cm^{-2}) is highlighted in gray.

Nevertheless, for these two sources we assume the lower-N_H, Compton-thin solutions on the basis that their X-ray-to-MIR luminosity ratios are consistent with those for unobscured AGNs (Section 5).

Considering all of the X-ray spectral constraints together, there are three sources with strong evidence for being CT AGNs (J0505, J1506, and J1512; two of which have supporting evidence from high equivalent width Fe Kα emission, as shown in Table 3), one likely CT AGN (J1534; supporting indirect evidence is presented in Section 5), one possible CT AGN (J1653; although the indirect evidence prefers a lower-obscuration solution; see Section 5), one highly obscured

Compton-thin AGN (J1410), one uncertain but likely highly obscured AGN (J0823), and one likely moderately absorbed AGN (J1444). Of the total four likely CT AGNs identified with *NuSTAR*, none would be identified as CT using just the soft X-ray ($<$10 keV) data, except possibly J0505, for which the *XMM-Newton* spectrum alone shows good evidence for a $\gtrsim$1 keV Fe Kα line.

Prior to this work, only one other AGN has been identified in the *NuSTAR* extragalactic surveys with strong evidence for CT absorption. This source, ID 330, was identified in the *NuSTAR*-COSMOS survey (Civano et al. 2015; Zappacosta et al. 2017). Like the robust CT AGNs presented here (J0505, J1506, and J1512), ID 330 lies at low redshift ($z = 0.044$) and has a high *NuSTAR* band ratio (see Figure 1). Assuming a BNTORUS-based model to fit the X-ray spectrum, the column density of ID 330 is $N_H = (1.2^{+0.3}_{-0.1}) \times 10^{24}$ cm^{-2} (Civano et al. 2015), which is similar to J0505 and less extreme than J1506 and J1512. Additional CT candidates are identified by Del Moro et al. (2017) and Zappacosta et al. (2017), as part of studies that focus on the broad X-ray spectral properties of *NuSTAR* extragalactic survey sources. We note that our extreme sample (selected from the total 40-month serendipitous catalog; see Section 2) does not overlap with the Zappacosta et al. (2017) sample, which is a subset of 24 serendipitous sources (plus 39 sources from the *NuSTAR* dedicated-field surveys).

5. Indirect Absorption Diagnostics

The intrinsic X-ray and MIR luminosities of AGNs are tightly correlated (e.g., Krabbe et al. 2001; Lutz et al. 2004; Horst et al. 2008; Fiore et al. 2009; Gandhi et al. 2009; Lanzuisi et al. 2009; Ichikawa et al. 2012; Matsuta et al. 2012; Asmus et al. 2015; Mateos et al. 2015; Stern 2015; Chen et al. 2017). The observed X-ray-to-MIR luminosity ratio of a source can therefore give an independent, albeit indirect, assessment of the degree of obscuration (e.g., see Alexander 2017, for a recent review); the *observed* X-ray luminosity for any significantly absorbed AGN will be suppressed with respect to the *intrinsic* luminosity, causing it to deviate from the X-ray-to-MIR luminosity relation. This diagnostic has been utilized for other *NuSTAR* studies of obscured AGNs (e.g., Baloković et al. 2014; Lansbury et al. 2014, 2015; Stern et al. 2014; Annuar et al. 2015, 2017; Gandhi et al. 2017; LaMassa et al. 2016).

Figure 6 shows the observed X-ray versus intrinsic 6 μm luminosities for the eight extreme *NuSTAR* serendipitous survey sources. Adopting the methodology of Assef et al. (2008, 2010, 2013), the AGN $L_{6\mu m}$ values have been determined using SED modeling of the SDSS and *WISE* photometry available, where each SED is modeled as the best-fit linear combination of four empirical templates (one AGN template and three different galaxy templates; Assef et al. 2010). The approach allows constraints on the relative contribution of the AGN and the host galaxy to the observed luminosity (see Lansbury et al. 2014, 2015, for applications of the same technique to an SDSS Type 2 quasar sample). For two of the extreme *NuSTAR* sources (J1444 and J1653) the SED modeling results are consistent with zero contribution from the AGN, and we therefore adopt conservative upper limits for $L_{6\mu m}$ (Figure 6). For the remaining six sources, the AGN contributes between $\approx$0.07 and $\approx$0.77 of the overall luminosity, for the 0.1–30 μm wavelength range (see
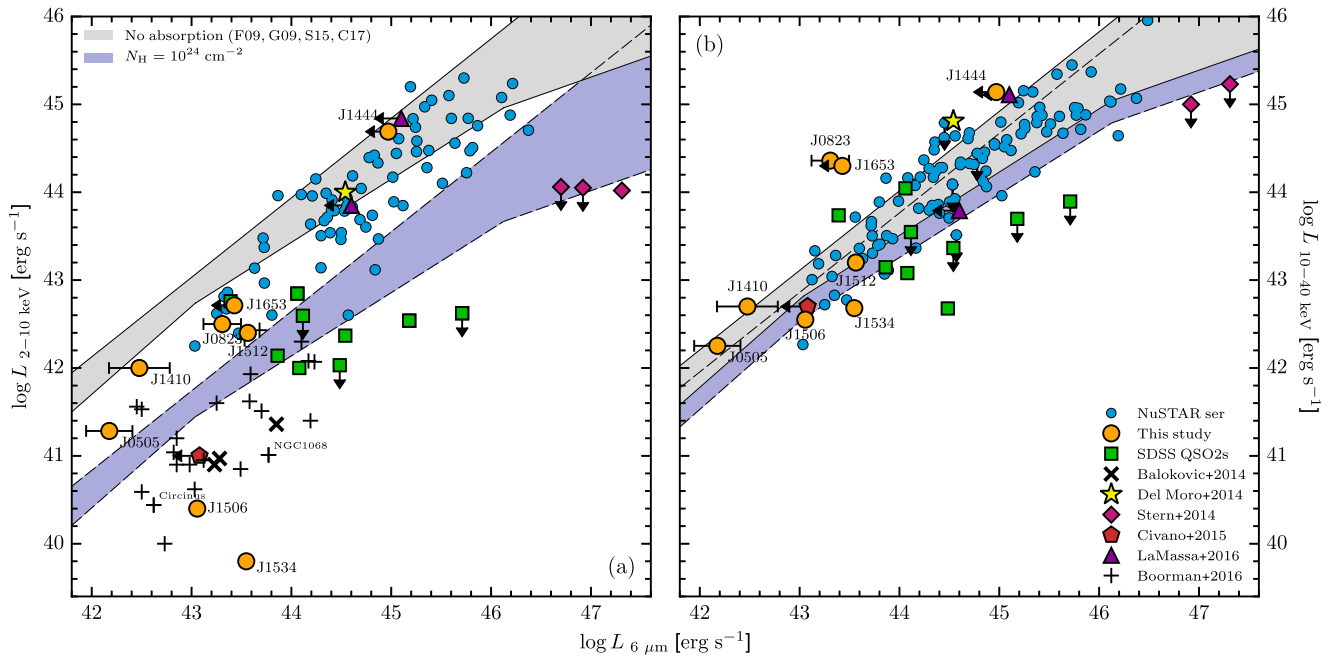
Figure 6. X-ray luminosities (at rest-frame 2–10 keV and 10–40 keV) vs. rest-frame 6 μm luminosity in νL_ν units ($L_{6\mu m}$). For the data points, we show observed X-ray luminosities (i.e., uncorrected for line-of-sight absorption of the X-rays). The extreme *NuSTAR* serendipitous survey sources are highlighted as orange circles and are individually labeled. We compare to "normal" *NuSTAR* serendipitous survey sources (smaller blue circles; Lansbury et al. 2017) and to other *NuSTAR*-observed samples of obscured to CT AGNs (see figure legend). We also compare with known "bona fide" CT AGNs in the local universe (plus signs; distance $\lesssim$ 100 Mpc; data compiled in P. G. Boorman et al. 2017, in preparation), including NGC 1068 and Circinus. The gray regions (with solid borders) highlight the range of luminosity ratios expected in the case of zero X-ray absorption (based on Fiore et al. 2009; Gandhi et al. 2009; Stern 2015; Chen et al. 2017), and the purple regions (with dashed borders) show the approximate X-ray suppression expected for absorption by gas with a column density of $N_{\rm H} = 10^{24}$ cm^{-2}.

Table 5
SED Modeling Results

| Object	$\hat{a}$	$L_{6\mu m}$ 10^{42} erg s^{-1}
(1)	(2)	(3)
J0505	0.07 ± 0.05	1.5 ± 0.8
J0823	0.28 ± 0.08	20.3 ± 8.8
J1410	0.11 ± 0.07	3.0 ± 2.1
J1444	$0.00^{+0.19}$	<933.2
J1506	0.28 ± 0.01	11.4 ± 0.7
J1512	0.76 ± 0.09	36.6 ± 1.7
J1534	0.40 ± 0.03	35.3 ± 3.8
J1653	$0.02^{+0.06}_{-0.02}$	<26.8

Note. Column (1): abbreviated *NuSTAR* source name. Column (2): fractional contribution of the AGN to the intrinsic luminosity at 0.1 μm–30 μm. Column (3): rest-frame 6 μm luminosity of the AGN.

Table 5). The resulting uncertainties on $L_{6\mu m}$ (also listed in Table 5) are determined from a Monte Carlo resampling of the photometric data over 1000 iterations and are shown in Figure 6.

In Figure 6 we compare with "normal" *NuSTAR* serendipitous survey sources (Lansbury et al. 2017) and with other *NuSTAR*-observed highly obscured AGNs, including nearby CT AGNs identified in the *NuSTAR* snapshot survey ($z \approx 0.01$; Baloković et al. 2014), candidate CT Type 2 quasars selected by SDSS ($z = 0.05$–0.49; Gandhi et al. 2014; Lansbury et al. 2014, 2015), a highly obscured quasar identified in the *NuSTAR*-ECDFS survey ($z \approx 2$; Del Moro et al. 2014), and the CT AGN identified in the

NuSTAR-COSMOS survey ($z = 0.044$; C15). Also plotted are "bona fide" CT AGNs in the local universe (distance $\lesssim$ 100 Mpc; data compiled in P. G. Boorman et al. 2017, in preparation). We compare all sources with the intrinsic X-ray–MIR relation for unobscured AGNs (Fiore et al. 2009; Gandhi et al. 2009; Stern 2015; Chen et al. 2017), and to demonstrate the expected deviation from the relation for highly obscured AGNs, we also show the modified relation for X-ray luminosities suppressed by $N_{\rm H} = 10^{24}$ cm^{-2} gas. The latter results in a more extreme suppression of the X-ray luminosity for the 2–10 keV band ($L_{\rm X}$ is decreased by a factor of $\approx$20) than for the 10–40 keV band (a factor of $\approx$2 decrease), where the higher-energy photons are less affected by absorption.

For the eight extreme *NuSTAR* serendipitous survey sources, the X-ray-to-MIR luminosity ratios are in broad agreement with the X-ray spectral modeling results, in that the sources with X-ray spectroscopic evidence for being CT are further offset from the intrinsic $L_{\rm X}$–$L_{\rm MIR}$ relations than the less obscured AGNs. This is especially apparent for J0505, J1506, J1512, and J1534 at 2–10 keV, where these likely CT sources overlap well with the X-ray-to-MIR luminosity ratios of local "bona fide" CT AGNs, as well as luminous highly obscured and CT Type 2 quasars. The $L_{\rm X}$–$L_{\rm MIR}$ ratios are very low in the cases of J1506 and J1534, which appear to lie even lower than local bona fide CT AGNs (including Circinus and NGC 1068), and have observed X-ray luminosities that are suppressed by $\approx$2–3 orders of magnitude. The X-ray properties of these *NuSTAR* sources (Section 4.2) suggest that the X-ray weakness is due to extreme absorption, rather than intrinsic X-ray weakness (e.g., Gallagher et al. 2001; Wu et al. 2011; Luo et al. 2014; Teng et al. 2015). J1653 has a relatively high ratio (at both 2–10 keV and 10–40 keV), suggesting a low column density that is in
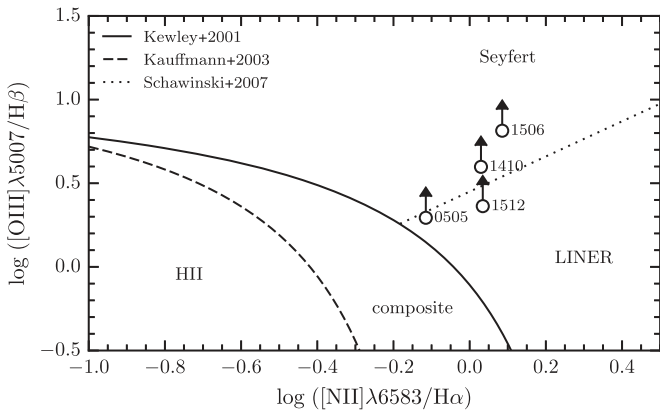
Figure 7. Emission-line ratios for the four sources where BPT diagnostics are possible. The solid line shows a theoretical maximum for starbursts (Kewley et al. 2001), the dashed line shows an empirical threshold to separate star-forming H II regions from AGNs (Kauffmann et al. 2003), and the dotted line shows an empirical threshold to distinguish between Seyfert AGNs and LINER classifications (Schawinski et al. 2007).

tension with the high value measured in Section 4. We note, however, that not all known CT AGNs have low L_X–L_{MIR} ratios, and a small fraction are even underluminous in MIR emission compared to the intrinsic relations (NGC 4945, for instance; e.g., Asmus et al. 2015), which may in part result from MIR extinction. Overall, our indirect analysis does not highlight any additional likely CT AGNs in the extreme serendipitous sample that were not already identified by the X-ray spectral analysis.

6. Optical Properties

6.1. Optical Spectra

For four of the eight extreme *NuSTAR* sources studied here, the optical spectra were obtained from our dedicated follow-up program with Keck (for J1444 and J1653; using the LRIS instrument), *Magellan* (J0823; using the IMACS instrument), and the NTT (J1512; using the EFOSC2 instrument).[37] Details of the observing runs and follow-up campaign are provided in Lansbury et al. (2017). For two sources (J1506 and J1534) the optical spectra are from the SDSS. For the remaining two sources (J0505 and J1410) the spectroscopic redshifts and spectra are from the 6dF survey (Jones et al. 2004, 2009) and the Anglo-Australian Telescope (AAT) observations of Radburn-Smith et al. (2006), respectively. The optical spectra are provided in the Appendix. The spectroscopic redshifts (see Table 1) are all robust, having been determined using 4–15 detected emission/absorption lines for each source (median of nine detected lines per source), except in the case of J1444, where the redshift solution is based on two weakly detected emission lines (most likely C IV and C III) at $z = 1.539$).

All of the optical spectra show narrow emission lines and have continua that appear consistent with being dominated by the host galaxy. In five cases (J0505, J1410, J1506, J1534, and J1653) the latter is confirmed by the identification of galactic absorption lines. These optical properties are congruous with the interpretation of these AGNs as obscured systems, in agreement with the X-ray constraints. To quantify the

emission-line properties, we fit the optical spectra for the major lines at rest frame 3500–7000 Å (e.g., [O II], Hβ, [O III], [O I], Hα, [N II], and [S II]) with the pyspeckit software following Berney et al. (2015) and the general procedure in Koss et al. (2017). We correct the narrow-line ratios (Hα/Hβ) assuming an intrinsic ratio of 3.1 and the Cardelli et al. (1989) reddening curve.

For six sources with significantly detected Hα emission lines (signal-to-noise ratio S/N $\gtrsim$ 4; J0505, J0823, J1410, J1506, J1512, and J1534), the Hα FWHMs range from 269 to 538 km s^{-1}, before correction for instrument resolution. In no case is a second (broad-line) component required to provide a statistically acceptable fit to the data. These results confirm the visual classifications of these sources as narrow-line systems (Lansbury et al. 2017). We note that J1653 has only a weak detection of Hα, and J1444 is at high redshift ($z = 1.539$) such that the above emission lines are not in the redshifted spectrum.

For four sources (J0505, J1410, J1506, and J1512), it is possible to apply AGN emission-line diagnostics (e.g., Kewley et al. 2006; Veilleux & Osterbrock 1987) using the [N II]/Hα and [O III]/Hβ emission-line flux ratio constraints. This is not possible for J0823, due to a gap in the spectrum, and for J1534 and J1653, due to the low S/N of the key emission lines. Figure 7 shows the location of the former four sources on the Baldwin–Phillips–Terlevich (BPT) diagram. All four sources fall into the AGN region based on the upper limits for the Hβ line, which is weak to undetected (S/N < 3). The weak Hβ line emission is likely due to extinction by dusty gas and has previously been observed for X-ray-selected obscured AGNs, particularly in mergers (e.g., Koss et al. 2016a, 2016b). We also note that Hβ is undetected for J0823, J1534, and J1653, and even [O III] is undetected in the case of J1534. The seven $z < 0.4$ extreme *NuSTAR* AGNs would thus be unidentified in any optical surveys requiring the detection of Hβ.

6.2. Host Galaxies

The five lower-redshift ($z < 0.2$) extreme *NuSTAR* sources (J0505, J1410, J1506, J1512, and J1534) have well-resolved host galaxies at optical wavelengths, while the higher-redshift sources are consistent with point-source emission. Four of the five lower-redshift sources are likely CT systems based on our X-ray analyses and also have relatively high quality optical coverage from Pan-STARRS (PS1; Chambers et al. 2016) or our own ESO-NTT imaging (see Figure 8). The other lower-redshift source (J1410), on the other hand, is Compton-thin and is limited to low-quality optical coverage from photo-graphic plate observations. Here we comment on the host galaxies, and nearby companion galaxies, for the lower-redshift sources.

J0505.—The optical counterpart is 2MFGC 04170, a highly inclined disk galaxy. The Pan-STARRS coverage of 2MFGC 04170 reveals spatially extended emission at $\approx$12″ offset (or a projected separation of $\approx$9 kpc) and at a position angle of $\approx$70°, which appears consistent with being a companion galaxy to 2MFGC 04170 (see Figure 8). We hereafter refer to this second companion source as J050601.2–235002.6. Since this source had no available redshift information, we performed follow-up spectroscopy with Keck (provided in the Appendix). We find that J050601.2–235002.6 lies at $z = 0.137$ and is therefore a

---

[37] *Magellan* program ID: CN2015A-87. NTT program ID: 093.B-0881.
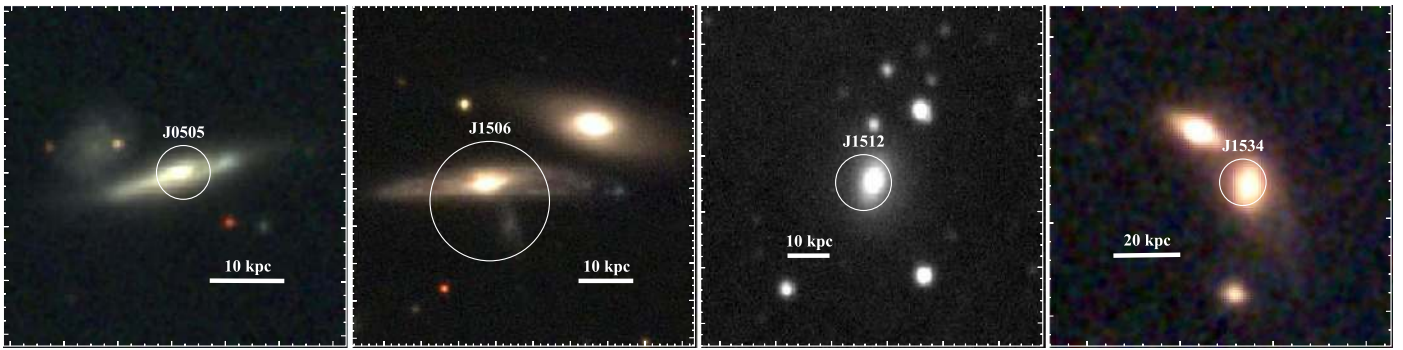
Figure 8. Optical images for the extreme *NuSTAR* sources that have both a high CT likelihood and a well-resolved host galaxy in the optical imaging. For J0505 (first panel; $z = 0.036$), J1506 (second panel; $z = 0.034$), and J1534 (fourth panel; $z = 0.160$) we use Pan-STARRS (*g*, *r*, and *i* band) color composites. For J1512 (third panel; $z = 0.069$) we use NTT *R*-band imaging from our follow-up program. The white circles mark the X-ray positions: for J1506 we show the *NuSTAR* positional error circle (16″ radius), while for J0505, J1512, and J1534 the circles mark the *XMM-Newton*, *Swift* XRT, and *Chandra* positions, respectively (5″, 5″, and 2.″5 radii shown, respectively). North is up and east is to the left. The major tick marks indicate 10″ offsets in R.A. (horizontal axes) and decl. (vertical axes). Two of these *NuSTAR*-identified likely CT AGNs (J1506 and J1534) belong to major mergers, with likely tidal features visible in both cases.

background galaxy that is coincidentally aligned along the line of sight, rather than being a merging companion to 2MFGC 04170.

J1506.—The optical counterpart is UGC 09710, an edge-on Sb spiral galaxy belonging to a close spiral–spiral galaxy pair in an early-stage major merger (see Figure 8), and separated from its similar mass partner galaxy (IC 1087; $z = 0.035$; S0-a type) by ≈ 16 kpc in projection (Yuan et al. 2012). Physical disturbances resulting from the major merger could potentially be related to an increase in the central gas content. In the Appendix we present a Palomar optical spectrum for the companion galaxy (IC 1087), which shows a possible AGN (also consistent with a LINER classification) with a dominant galaxy continuum. [O III] and Hβ are undetected for the companion galaxy (presumably due to host galaxy dilution), and the [N II]:Hα line strength ratio is very high, but is likely affected by stellar absorption. For this companion galaxy, there is no additional evidence from the *WISE* colors for an AGN, and the source is undetected in the current X-ray coverage.

J1410.—The available photographic plate coverage (from the UK Schmidt Telescope) shows an extended host galaxy, but the low data quality precludes type and disturbance classifications. Nevertheless, there do not appear to be any nearby (massive) companion galaxies.

J1512.—We have obtained *R*-band imaging with the ESO-NTT (shown in Figure 8), which is in visual agreement with the host being a relatively undisturbed early-type galaxy. The neighboring optical sources are consistent with being unresolved point sources, with FWHMs similar to the seeing ($\approx 1.''5$), and are therefore unlikely to be associated with J1512.

J1534.—The Pan-STARRS imaging (Figure 8) shows good evidence that the optical host galaxy (SDSS J153445.80 +233121.2; $z = 0.160$) is undergoing a major merger with a narrowly offset companion galaxy (SDSS J153446.19 +233127.1; no spec-*z*); the respective galaxy nuclei are separated by $\approx 8''$ (or ≈ 22 kpc in projection), and likely extended tidal features are visible. The merger stage is not clear. We present Palomar spectroscopic follow-up for the
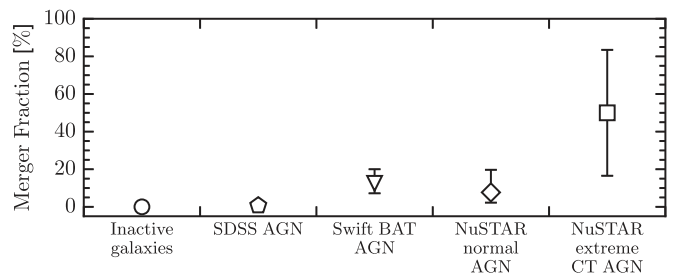
Figure 9. Fraction of host galaxies in major mergers, for *NuSTAR* serendipitous survey sources at $z < 0.2$. The fraction is shown for two subsets of the serendipitous survey: (1) the extreme AGNs (square) with very hard X-ray spectra and evidence for CT obscuration (J0505, J1506, J1512, and J1534, i.e., those discussed in this work) and (2) "normal" *NuSTAR* AGNs (diamond). We also compare to the major-merger fraction for *Swift* BAT AGNs (triangle; Koss et al. 2010) and those for inactive galaxies and SDSS AGNs matched to the *Swift* BAT sample (circle and pentagon, respectively; Koss et al. 2010; the error bars are smaller than the data points). Uncertainties are shown at the 90% confidence level.

companion galaxy in the Appendix, although there are no significantly detected emission or absorption features.

A notable feature of the galaxies is that both J0505 and J1506 have close to edge-on geometries, which could contribute at least some of the observed X-ray obscuration. The axis ratios of the host galaxies are $b/a = 0.24$ and 0.23 for J0505 and J1506, respectively, based on isophotal fitting of the galaxy images in Figure 8 (using the IRAF task `ellipse`). The remaining two likely CT sources (J1512 and J1534), on the other hand, have axis ratios exceeding $b/a = 0.6$. Although the source numbers are currently small, the above implies a relatively high fraction ($50\% \pm 33\%$) of close to edge-on systems for CT AGNs selected by *NuSTAR*. For comparison, only $\approx 16\%$ of the general hard-X-ray-selected AGN population have $b/a < 0.3$, based on isophotal analyses for the *Swift* BAT AGN sample (Koss et al. 2011). Although the difference is only weakly significant, a similar result has also been reported for CT AGNs selected with *Swift* BAT (Koss et al. 2016a). Other studies, however, find that edge-on galaxy inclinations are not clearly related to CT absorption (e.g., Annuar et al. 2017; Buchner & Bauer 2017).

6.2.1. A High Fraction of Galaxy Mergers for the Compton-thick AGNs?

It is interesting that two of the four likely CT AGNs (J0505, J1506, J1512, and J1534) are hosted by galaxy major mergers (see Figure 8). To assess the statistical significance of the apparently high merger fraction for these extreme *NuSTAR* serendipitous survey AGNs ($f_{merger} = 50 \pm 33\%$; the errors represent binomial uncertainties), we can search for similar merging systems in the sample of nonextreme (or "normal") serendipitous survey AGNs. To this end, from the overall serendipitous survey sample, we apply a cut of $BR_{Nu} < 1.7$, thus limiting to those sources that do not have very hard *NuSTAR* spectra (based on the BR_{Nu} threshold in Section 2). We limit this comparison sample to source redshifts of $0.01 < z < 0.2$, thus matching the redshift range of the four extreme sources. We exclude two sources from the sample that are likely strongly associated with the science targets of their *NuSTAR* observations (similar to the exclusion of J2028 from the extreme sample; see Section 2). These cuts leave 36 normal *NuSTAR* sources. Finally, we limit the sample to the 26 (out of 36) sources that are covered by Pan-STARRS observations and therefore have optical coverage that is of comparable quality to the four extreme *NuSTAR* sources. As a result, the comparison of visual merger classifications between the two different samples is unlikely to be significantly affected by variations in optical imaging sensitivity. The comparison sample is matched in X-ray luminosity distribution to the extreme *NuSTAR* AGNs (with a Kolmogorov–Smirnov test *p*-value of 0.8).

Of the 26 normal AGNs, we identify one that has evidence for a galaxy major merger, with a comparably sized companion galaxy lying at the same redshift and offset by a projected distance of ≈ 25 kpc. There are an additional two normal AGNs with possible evidence for mergers, although the candidate companion galaxies are relatively small in size, with unknown redshifts. We conservatively assume that two of the normal AGNs are in major mergers with <30 kpc separation companions. Our estimate for the major-merger fraction of normal *NuSTAR* AGNs is therefore $f_{merger} = 8^{+12}_{-5}\%$. This is in agreement with the (<30 kpc separation) major-merger fraction for *Swift* BAT AGNs ($f_{merger} = 13^{+7}_{-5}\%$; Koss et al. 2010). Figure 9 compares the above merger fractions. We additionally compare with low-redshift inactive galaxies and optical Type 2 AGNs (both from the SDSS), which are matched to the *Swift* BAT sample (Koss et al. 2010) and have very low merger fractions compared to the *Swift* BAT and extreme *NuSTAR* AGNs. At low significance levels of 1.8σ and 1.7σ (according to the Fisher exact probability test), the extreme (very hard, CT) *NuSTAR* AGNs have a higher merger fraction than both the normal *NuSTAR* AGNs and the *Swift* BAT AGNs, respectively. This could be a result of Compton-thick phases of black hole growth being more strongly linked (than less obscured phases) to the merger stage of the galaxy evolutionary sequence.

The above result is of interest given recent findings for other AGN samples. Kocevski et al. (2015) find evidence that highly obscured ($N_H \gtrsim 3 \times 10^{23}\,cm^{-2}$) AGNs at $z \sim 1$ have a higher frequency of merger/interaction morphologies relative to less obscured AGNs matched in redshift and luminosity. Furthermore, Koss et al. (2016a) noted a high close (<10 kpc) merger fraction for likely CT *Swift* BAT
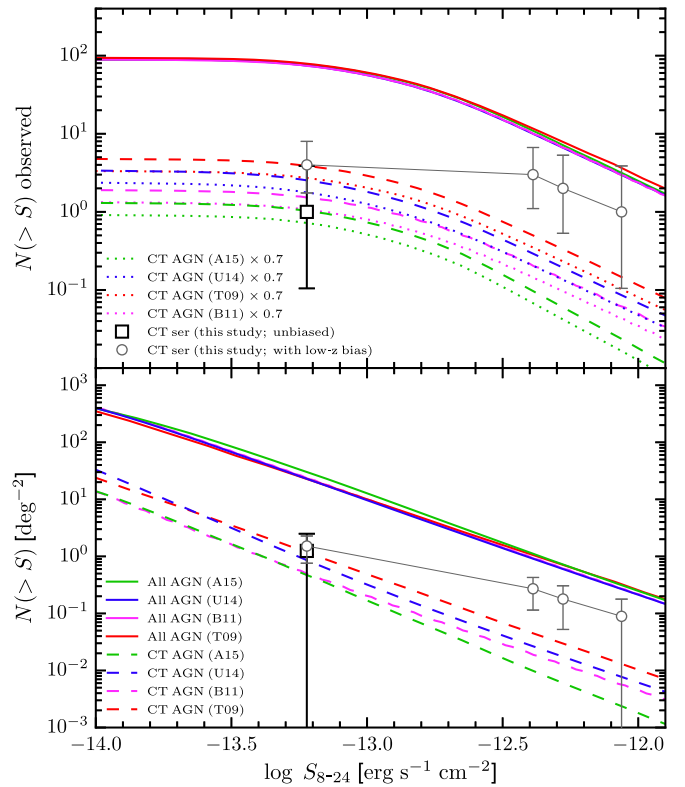

Figure 10. Top panel: observed cumulative number counts (and 90% CL uncertainties), as a function of 8–24 keV flux (S_{8-24}), for the CT AGNs identified in the *NuSTAR* serendipitous survey. The gray circles show the number counts for all four CT AGNs. The black square shows the modified number counts when removing the three low-redshift CT AGNs (J0505, J1506, and J1512; see Section 7). We compare to predicted tracks for CT AGNs (dashed lines) and all AGNs (solid lines) based on the models of A15, U14, B11, and T09. The dotted lines show modifications of the CT model tracks to account for the spectroscopic incompleteness of the serendipitous survey. Bottom panel: "intrinsic" cumulative number density (and 68% CL uncertainties) as a function of flux.

AGNs at $z \lesssim 0.03$ ($f_{merger} = 22\%$; i.e., 2/9). The recent study of Ricci et al. (2017) indicates a possible connection between the late stages of galaxy mergers and high AGN obscuration, in a sample of local luminous and ultraluminous infrared galaxies (U/LIRGs), using a combination of dedicated and archival X-ray observations. Taken together, the results may suggest a departure from simple orientation-based unified models of AGN obscuration and indicate an evolutionary scenario where highly obscured phases of black hole growth can be associated with a merger-driven increase in the circumnuclear gas content (e.g., Sanders et al. 1988; Draper & Ballantyne 2010; Treister et al. 2010). An increased sample size and deeper imaging would help to further test the CT AGN–merger connection using the *NuSTAR* serendipitous survey.

7. The Prevalence of Compton-thick Absorption

We have taken advantage of the relatively large sample size of the *NuSTAR* serendipitous survey to identify rare highly obscured AGNs. While all of the eight extreme sources investigated are consistent with being highly obscured, four in
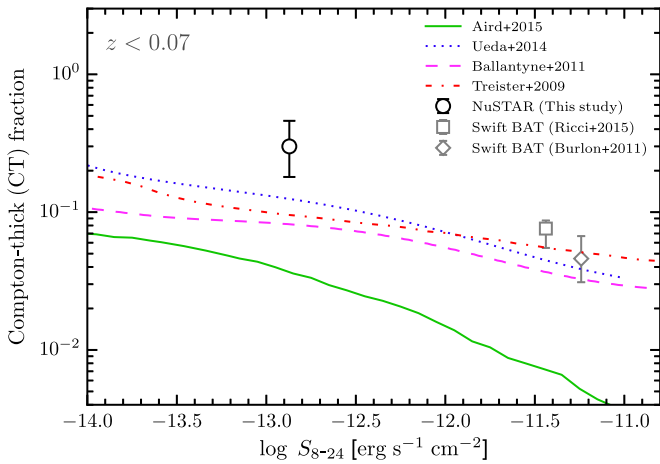
Figure 11. Observed CT fraction (relative to all AGNs) as a function of 8–24 keV flux limit, for $z < 0.07$. The black circle data point shows the *NuSTAR* serendipitous survey constraint from this work. The gray data points show constraints using the 3 yr (diamond; Burlon et al. 2011) and 70-month (square; Ricci et al. 2015) *Swift* BAT surveys, respectively. We compare with model predictions based on A15 (green solid line), U14 (blue dotted line), B11 (pink dashed line), and T09 (red dot-dashed line).

particular are likely CT (J0505, J1506, J1512, and J1534). A fifth source (J1653) is a CT candidate based on the X-ray analysis, but this result is in tension with the indirect constraints (see Section 5). Here we assess how the observed number of CT AGNs in the *NuSTAR* serendipitous survey compares with the number expected from AGN population models, which are informed by the results from previous (primarily <10 keV) X-ray surveys. We consider the hard-band (8–24 keV) selected serendipitous survey sample, since this is the energy band in which *NuSTAR* is uniquely sensitive, and Galactic latitudes of $|b| > 10°$ (i.e., out of the Galactic plane). We conservatively exclude J1653. The top panel of Figure 10 shows the observed (cumulative) number of CT sources as a function of limiting flux, and these results are compared to model predictions for the observed numbers of CT AGNs and all AGNs. For these predictions, we fold the area-sensitivity curve of the serendipitous survey through models for the evolution of the X-ray luminosity function (XLF) and the N_H distribution of AGNs, from Treister et al. (2009, hereafter T09), Ueda et al. (2014, hereafter U14), Aird et al. (2015, hereafter A15), and the updated version of Ballantyne et al. (2011, hereafter B11). The updates to the B11 model are summarized in Harrison et al. (2016). We additionally show, in the bottom panel of Figure 10, the "intrinsic" cumulative number densities (i.e., the sky number counts before accounting for the survey sensitivity; $N(>S)$, in units of deg^{-2}).

In Figure 10 the gray circle data points show the number counts for all four CT AGNs. There is an apparent excess in the CT number counts at high fluxes, compared to the model predictions. This excess may be expected given that the three lowest-redshift, highest-flux sources (J0505, J1506, and J1512; $z < 0.07$) show evidence for being weakly associated with the *Swift* BAT AGN targets of the *NuSTAR* observations (see Section 2.1), and also given that galaxy clustering tends to be high around BAT AGNs (e.g., Cappelluti et al. 2010; Koss et al. 2010). In Figure 10 we also show the CT number counts using J1534 only (i.e., excluding J0505, J1506, and J1512;

black square data point). Although not particularly constraining, this brings the number counts into better agreement with all of the models (T09, B11, U14, A15, and Gilli et al. 2007), suggesting consistency with a wide range of intrinsic CT fractions[38] ranging from $f_{CT} \approx 10\%$–40%, at least for $z > 0.07$. For comparison, Zappacosta et al. (2017) study the X-ray spectral properties of *NuSTAR* extragalactic survey sources and find that the range of CT fractions allowed by their sample is broad ($f_{CT} \approx 10\%$–70%). The *NuSTAR* survey constraints on f_{CT} are therefore in broad agreement with $z \gtrsim 0.1$ constraints from soft (<10 keV) X-ray observatories ($f_{CT} \approx 30\%$–50%; e.g., Brightman & Ueda 2012; Brightman et al. 2014; Buchner et al. 2015).

However, it is important to consider independently the low-redshift ($z < 0.07$) regime, where we have detected the highest numbers of CT AGNs. Although the overall number counts in this regime may have an upward excess with respect to model predictions (as mentioned above), the CT *fraction* should be unaffected. The observed CT fraction for the $z < 0.07$ *NuSTAR* serendipitous survey sample is $f_{CT}^{obs} = 30^{+16}_{-12}\%$ (68% CL binomial uncertainties). The intrinsic X-ray luminosity range of this subsample is $41.3 < \log(L_{10-40\,keV}/\mathrm{erg\,s^{-1}}) < 44.0$. Figure 11 compares our observational constraint to model predictions as a function of 8–24 keV flux. We find a higher CT fraction than is expected from the models. The difference is statistically significant in one case ($>3\sigma$; comparing to A15) and at lower significance levels for the remaining models ($<3\sigma$; comparing to T09, B11, and U14). In Figure 11 we additionally compare with data points for the higher-flux *Swift* BAT survey (Burlon et al. 2011; Ricci et al. 2015), for which we have converted to the 8–24 keV *NuSTAR* band assuming $\Gamma_{eff} = 1.9$. At present, the origin of the high observed CT fraction at $z < 0.07$ is unclear. A likely explanation is that the current models are not well constrained for the new parameter space probed with *NuSTAR*, in which case the AGN population models require updating. An alternative possibility, however, is that f_{CT}^{obs} is boosted owing to a real connection between CT absorption and the large-scale environment, in combination with *NuSTAR* having preferentially targeted (at $z < 0.07$) fields with relatively high galaxy densities (e.g., fields around *Swift* BAT AGNs).

Finally, we note that the number of CT AGNs presented here could be a lower limit to the total number within the *NuSTAR* serendipitous survey as there are additional sources, not included in this work, that have band-ratio limits consistent with a large range in column density (e.g., see Figure 1), and any CT sources with relatively soft spectral shapes could potentially be missed by our initial selection (Section 2). Alternative approaches (e.g., detailed X-ray or multiwavelength analyses of the broader sample) may tease out additional CT AGNs within the sample. However, large improvements on the constraints presented here will require further survey data from sensitive hard X-ray missions. Further data will be provided by the continued *NuSTAR* operations, which are likely to increase the serendipitous sample to $\gtrsim 1000$ sources, and potentially by future high-sensitivity >10 keV observatories (e.g., the *High-Energy X-ray Probe*, or *HEX-P*, mission concept currently under study; PI F. Harrison; see Brandt & Alexander 2015, for a brief overview).

---

[38] The CT fraction is defined here as the fraction of all AGNs that are CT.

8. Summary

In this paper we have searched for the most extreme sources in the *NuSTAR* serendipitous survey, in terms of having very hard spectral slopes (BR$_{Nu}$ ⩾ 1.7). The eight selected sources are all candidates for being highly obscured AGNs. A detailed look at the broadband (0.5–24 keV) X-ray data available, as well as the multiwavelength properties of these sources, has yielded the following main results.

1. The X-ray spectral analyses find that three of the extreme *NuSTAR* sources (J0505, J1506, and J1512) are newly identified robust Compton-thick (CT) AGNs at low redshift ($z < 0.1$). An additional source at higher redshift (J1534) is likely CT. The remaining four extreme sources are consistent with being CT or at least moderately absorbed; see Section 4.2.

2. Most (three out of four) of the likely CT AGNs identified with *NuSTAR* would not have been identified as highly obscured systems based on the low-energy (<10 keV) X-ray coverage alone. J1506 is a notable example: a newly uncovered CT AGN in the nearby universe ($z = 0.034$; $N_H > 2 \times 10^{24}$ cm^{-2}; $L_X \approx 2 \times 10^{43}$ erg s^{-1}), hosted by a previously known galaxy major merger; see Sections 4.2 and 6.2.

3. For all eight extreme sources, the optical spectra show evidence for narrow-line AGNs or galaxy-dominated spectra, supporting the X-ray classifications as obscured and CT AGNs; see Section 6.1. Measurements of the X-ray-to-MIR luminosity ratio, an indirect absorption diagnostic, are also broadly congruent with the X-ray classifications. Two sources (J1506 and J1534) have particularly extreme ratios, lying even lower in L_X/L_{MIR} than the well-known CT AGNs in the local universe; see Section 5.

4. A high fraction ($50\% \pm 33\%$) of the likely CT AGNs are hosted by galaxy major mergers. This is higher than the major-merger fractions for "normal" *NuSTAR* serendipitous survey sources and for *Swift* BAT AGNs, at a low significance level, motivating larger future studies; see Section 6.2.

5. We estimate the number counts of CT AGNs for the hard-band (8–24 keV) selected serendipitous survey sample at $|b| > 10°$. The number counts are broadly harmonious with AGN population models over the main redshift range of the survey ($0.1 \lesssim z \lesssim 2$), but there is disagreement at low redshifts ($z < 0.07$) where we find evidence for a high observed CT fraction of $f_{CT}^{obs} = 30^{+16}_{-12}\%$; see Section 7.

Appendix

A.1. Optical Spectra for the Extremely Hard NuSTAR Serendipitous Survey Sources

Here we provide the optical spectra (Figure 12) for the eight extreme *NuSTAR* AGNs, which are discussed in Section 6.1. The identified emission and absorption lines are highlighted in Figure 12 and are tabulated in Appendix A.2 of Lansbury et al. (2017).

### A.2. Optical Spectra for Companion Galaxies

A.2.1. J0505

As described in the main text, with the Keck telescope we performed optical spectroscopy for J050601.2−235002.6, the apparent companion galaxy to 2MFGC 04170 (the host galaxy for J0505). The resulting spectrum is shown in Figure 13. The relatively high redshift ($z = 0.137$) confirms that this is a background galaxy and a chance alignment with 2MFGC 04170 ($z = 0.036$).

A.2.2. J1506

As described in the main text, J1506 belongs to one of two galaxies in a major merger. With the Hale telescope at Palomar Observatory we performed optical spectroscopy for the companion galaxy (known as IC 1087). The resulting spectrum is shown in Figure 14.

A.2.3. J1534

As described in the main text, J1534 (hosted by galaxy SDSS J153445.80+233121.2) appears to be undergoing a major merger with a neighboring galaxy (SDSS J153446.19+233127.1). Since no spectroscopic redshift is available for the latter galaxy, we performed optical spectroscopy with the Hale telescope at Palomar Observatory, the spectrum from which is shown in Figure 15. Since no clear emission or absorption features are detected, this companion requires deeper spectroscopic observations in the future to reliably determine the redshift.
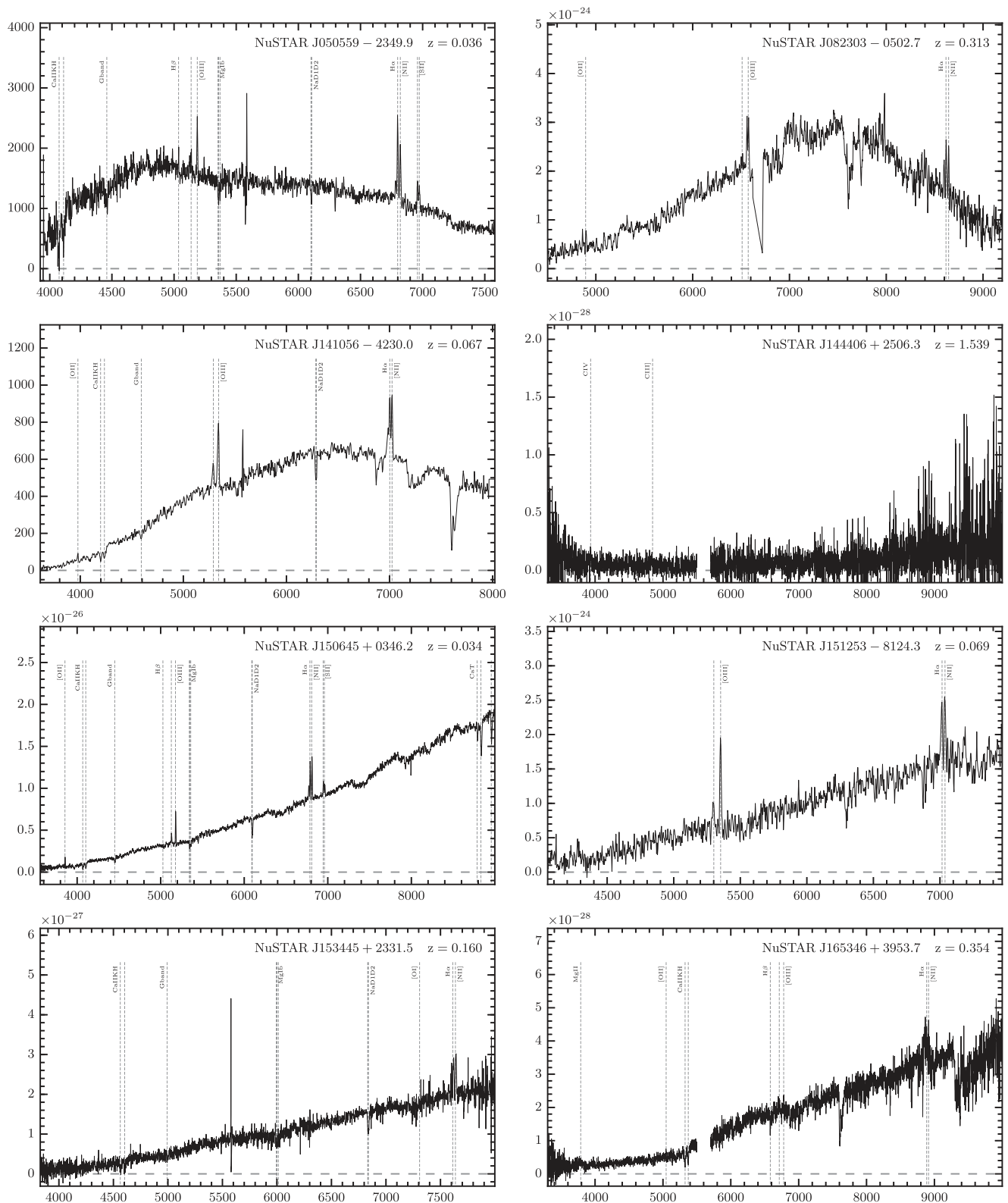
Figure 12. Optical spectra for the extreme *NuSTAR* serendipitous survey sources. The horizontal axis shows the observed-frame wavelength in units of Å. The vertical axis shows the flux (f_ν) in units of erg s^{-1} cm^{-2} Hz^{-1} for all sources except J0505 and J1410, for which the vertical axis shows the counts. The vertical dashed gray lines mark the emission and absorption lines identified.
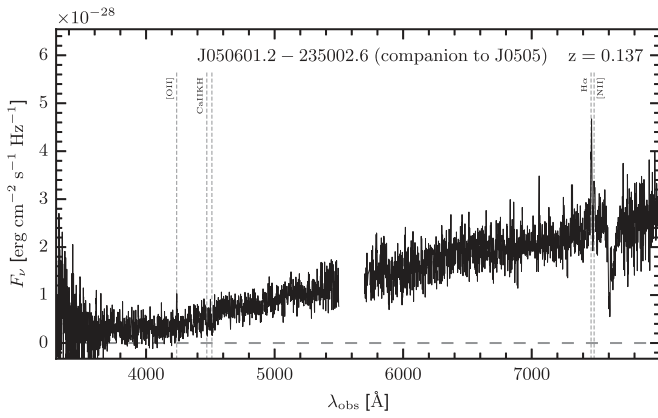
Figure 13. Keck optical spectrum for J050601.2–235002.6, the apparent companion galaxy to 2MFGC 04170 (the host galaxy for J0505). Multiple emission and absorption lines are identified and labeled here.
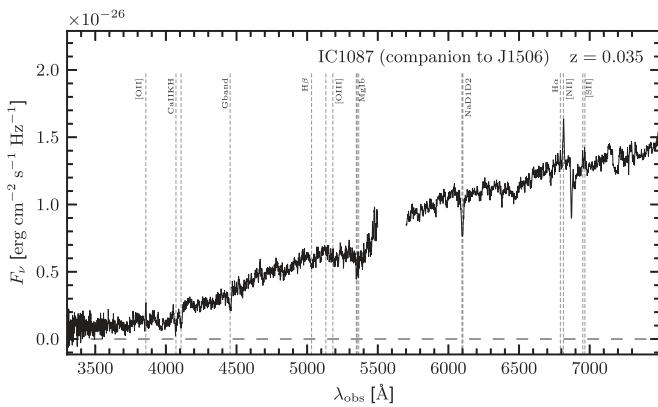
Figure 14. Palomar optical spectrum for IC 1087, the merging companion galaxy to UGC 09710 (the host galaxy for our lowest-redshift extreme *NuSTAR* source, J1506). Multiple emission and absorption lines are identified and labeled here.
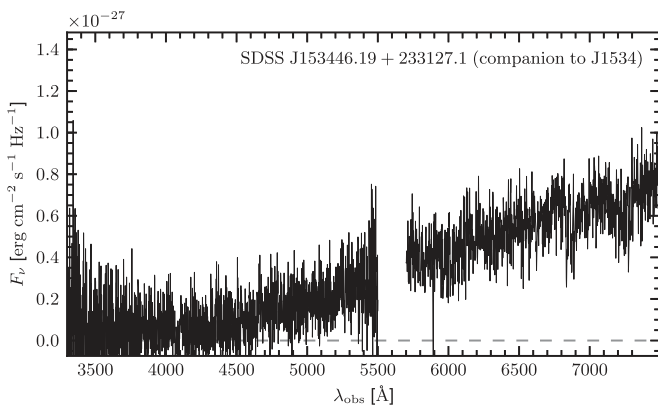
Figure 15. Palomar optical spectrum for SDSS J153446.19+233127.1, the merging companion galaxy to SDSS J153445.80+233121.2 (the host galaxy for J1534). The continuum is detected, although no clear emission or absorption lines are identified, precluding a spectroscopic redshift measurement.

ORCID iDs

G. B. Lansbury ⬤ https://orcid.org/0000-0002-5328-9827
J. Aird ⬤ https://orcid.org/0000-0003-1908-8463
P. Gandhi ⬤ https://orcid.org/0000-0003-3105-2615
D. Stern ⬤ https://orcid.org/0000-0003-2686-9241
M. Koss ⬤ https://orcid.org/0000-0002-7998-9581

I. Lamperti ⬤ https://orcid.org/0000-0003-3336-5498
M. Ajello ⬤ https://orcid.org/0000-0002-6584-1703
A. Annuar ⬤ https://orcid.org/0000-0003-0387-1429
R. J. Assef ⬤ https://orcid.org/0000-0002-9508-3667
D. R. Ballantyne ⬤ https://orcid.org/0000-0001-8128-6976
A. Comastri ⬤ https://orcid.org/0000-0003-3451-9970
F. A. Harrison ⬤ https://orcid.org/0000-0003-2992-8024
S. Marchesi ⬤ https://orcid.org/0000-0001-5544-0749
A. Masini ⬤ https://orcid.org/0000-0002-7100-9366
J. R. Mullaney ⬤ https://orcid.org/0000-0002-3126-6712
C. Ricci ⬤ https://orcid.org/0000-0001-5231-2645
J. A. Tomsick ⬤ https://orcid.org/0000-0001-5506-9855
D. J. Walton ⬤ https://orcid.org/0000-0001-5819-3552

References

Aird, J., Coil, A. L., Georgakakis, A., et al. 2015, MNRAS, 451, 1892
Aird, J., Coil, A. L., & Georgakakis, A. 2017, MNRAS, 465, 3390
Akylas, A., Georgantopoulos, I., Ranalli, P., et al. 2016, A&A, 594, A73
Alexander, D. M. 2017, AN, 338, 172
Alexander, D. M., Chary, R.-R., Pope, A., et al. 2008, ApJ, 687, 835
Alexander, D. M., & Hickox, R. C. 2012, NewAR, 56, 93
Alexander, D. M., Stern, D., Del Moro, A., et al. 2013, ApJ, 773, 125
Allevato, V., Finoguenov, A., Cappelluti, N., et al. 2011, ApJ, 736, 99
Allevato, V., Finoguenov, A., Civano, F., et al. 2014, ApJ, 796, 4
Annuar, A., Alexander, D. M., Gandhi, P., et al. 2017, ApJ, 836, 165
Annuar, A., Gandhi, P., Alexander, D. M., et al. 2015, ApJ, 815, 36
Antonucci, R. 1993, ARA&A, 31, 473
Arnaud, K. A. 1996, in ASP Conf. Ser. 101, Astronomical Data Analysis Software and Systems, ed. G. H. Jacoby & J. Barnes (San Francisco, CA: ASP), 17
Asmus, D., Gandhi, P., Hönig, S. F., Smette, A., & Duschl, W. J. 2015, MNRAS, 454, 766
Assef, R. J., Kochanek, C. S., Brodwin, M., et al. 2008, ApJ, 676, 286
Assef, R. J., Kochanek, C. S., Brodwin, M., et al. 2010, ApJ, 713, 970
Assef, R. J., Stern, D., Kochanek, C. S., et al. 2013, ApJ, 772, 26
Awaki, H., Murakami, H., Ogawa, Y., & Leighly, K. M. 2006, ApJ, 645, 928
Ballantyne, D. R. 2017, MNRAS, 464, 626
Ballantyne, D. R., Draper, A. R., Madsen, K. K., Rigby, J. R., & Treister, E. 2011, ApJ, 736, 56
Baloković, M., Comastri, A., Harrison, F. A., et al. 2014, ApJ, 794, 111
Berney, S., Koss, M., Trakhtenbrot, B., et al. 2015, MNRAS, 454, 3622
Brandt, W. N., & Alexander, D. M. 2015, A&ARv, 23, 1
Brightman, M., & Nandra, K. 2011, MNRAS, 413, 1206
Brightman, M., Nandra, K., Salvato, M., et al. 2014, MNRAS, 443, 1999
Brightman, M., & Ueda, Y. 2012, MNRAS, 423, 702
Buchner, J., & Bauer, F. E. 2017, MNRAS, 465, 4348
Buchner, J., Georgakakis, A., Nandra, K., et al. 2015, ApJ, 802, 89
Burlon, D., Ajello, M., Greiner, J., et al. 2011, ApJ, 728, 58
Cappelluti, N., Ajello, M., Burlon, D., et al. 2010, ApJL, 716, L209
Cappi, M., Panessa, F., Bassani, L., et al. 2006, A&A, 446, 459
Cardelli, J. A., Clayton, G. C., & Mathis, J. S. 1989, ApJ, 345, 245
Chambers, K. C., Magnier, E. A., Metcalfe, N., et al. 2016, arXiv:1612.05560
Chen, C.-T. J., Hickox, R. C., Goulding, A. D., et al. 2017, ApJ, 837, 145
Civano, F., Hickox, R. C., Puccetti, S., et al. 2015, ApJ, 808, 185
Civano, F., Mignoli, M., Comastri, A., et al. 2007, A&A, 476, 1223
Comastri, A., Ranalli, P., Iwasawa, K., et al. 2011, A&A, 526, L9
Comastri, A., Setti, G., Zamorani, G., & Hasinger, G. 1995, A&A, 296, 1
Daddi, E., Alexander, D. M., Dickinson, M., et al. 2007, ApJ, 670, 173
Del Moro, A., Alexander, D. M., Aird, J. A., et al. 2017, ApJ, in press
Del Moro, A., Alexander, D. M., Bauer, F. E., et al. 2016, MNRAS, 456, 2105
Del Moro, A., Mullaney, J. R., Alexander, D. M., et al. 2014, ApJ, 786, 16
Della Ceca, R., Severgnini, P., Caccianiga, A., et al. 2008, MmSAI, 79, 65
DiPompeo, M. A., Hickox, R. C., & Myers, A. D. 2016, MNRAS, 456, 924
DiPompeo, M. A., Myers, A. D., Hickox, R. C., Geach, J. E., & Hainline, K. N. 2014, MNRAS, 442, 3443
Donoso, E., Yan, L., Stern, D., & Assef, R. J. 2014, ApJ, 789, 44
Draper, A. R., & Ballantyne, D. R. 2010, ApJL, 715, L99
Fiore, F., Grazian, A., Santini, P., et al. 2008, ApJ, 672, 94
Fiore, F., Puccetti, S., Brusa, M., et al. 2009, ApJ, 693, 447
Fruscione, A., McDowell, J. C., Allen, G. E., et al. 2006, Proc. SPIE, 6270, 62701V
Gallagher, S. C., Brandt, W. N., Laor, A., et al. 2001, ApJ, 546, 795

Gandhi, P., Annuar, A., Lansbury, G. B., et al. 2017, MNRAS, 467, 4606
Gandhi, P., Horst, H., Smette, A., et al. 2009, A&A, 502, 457
Gandhi, P., Lansbury, G. B., Alexander, D. M., et al. 2014, ApJ, 792, 117
Gilli, R., Comastri, A., & Hasinger, G. 2007, A&A, 463, 79
Harrison, F. A., Aird, J., Civano, F., et al. 2016, ApJ, 831, 185
Harrison, F. A., Craig, W. W., Christensen, F. E., et al. 2013, ApJ, 770, 103
Hopkins, P. F., Hernquist, L., Cox, T. J., & Kereš, D. 2008, ApJS, 175, 356
Horst, H., Gandhi, P., Smette, A., & Duschl, W. J. 2008, A&A, 479, 389
Ichikawa, K., Ueda, Y., Terashima, Y., et al. 2012, ApJ, 754, 45
Jia, J., Ptak, A., Heckman, T., & Zakamska, N. L. 2013, ApJ, 777, 27
Jones, D. H., Read, M. A., Saunders, W., et al. 2009, MNRAS, 399, 683
Jones, D. H., Saunders, W., Colless, M., et al. 2004, MNRAS, 355, 747
Kalberla, P. M. W., Burton, W. B., Hartmann, D., et al. 2005, A&A, 440, 775
Kauffmann, G., Heckman, T. M., Tremonti, C., et al. 2003, MNRAS, 346, 1055
Kewley, L. J., Dopita, M. A., Sutherland, R. S., Heisler, C. A., & Trevena, J. 2001, ApJ, 556, 121
Kewley, L. J., Groves, B., Kauffmann, G., & Heckman, T. 2006, MNRAS, 372, 961
Kocevski, D. D., Brightman, M., Nandra, K., et al. 2015, ApJ, 814, 104
Koss, M., Mushotzky, R., Veilleux, S., et al. 2011, ApJ, 739, 57
Koss, M., Mushotzky, R., Veilleux, S., & Winter, L. 2010, ApJL, 716, L125
Koss, M., Trakhtenbrot, B., Ricci, C., et al. ApJ, in press (arXiv:1707.08123)
Koss, M. J., Assef, R., Baloković, M., et al. 2016a, ApJ, 825, 85
Koss, M. J., Glidden, A., Baloković, M., et al. 2016b, ApJL, 824, L4
Krabbe, A., Böker, T., & Maiolino, R. 2001, ApJ, 557, 626
Lacy, M., Storrie-Lombardi, L. J., Sajina, A., et al. 2004, ApJS, 154, 166
LaMassa, S. M., Ricarte, A., Glikman, E., et al. 2016, ApJ, 820, 70
LaMassa, S. M., Yaqoob, T., Ptak, A. F., et al. 2014, ApJ, 787, 61
Lansbury, G. B., Alexander, D. M., Del Moro, A., et al. 2014, ApJ, 785, 17
Lansbury, G. B., Gandhi, P., Alexander, D. M., et al. 2015, ApJ, 809, 115
Lansbury, G. B., Stern, D., Aird, J., et al. 2017, ApJ, 836, 99
Lanzuisi, G., Piconcelli, E., Fiore, F., et al. 2009, A&A, 498, 67
Lanzuisi, G., Ranalli, P., Georgantopoulos, I., et al. 2015, A&A, 573, A137
Luo, B., Brandt, W. N., Alexander, D. M., et al. 2014, ApJ, 794, 70
Lutz, D., Maiolino, R., Spoon, H. W. W., & Moorwood, A. F. M. 2004, A&A, 418, 465
Madsen, K. K., Harrison, F. A., Markwardt, C. B., et al. 2015, ApJS, 220, 8

Magdziarz, P., & Zdziarski, A. A. 1995, MNRAS, 273, 837
Masini, A., Comastri, A., Puccetti, S., et al. 2017, A&A, 597, A100
Mateos, S., Alonso-Herrero, A., Carrera, F. J., et al. 2012, MNRAS, 426, 3271
Mateos, S., Carrera, F. J., Alonso-Herrero, A., et al. 2015, MNRAS, 449, 1422
Matsuta, K., Gandhi, P., Dotani, T., et al. 2012, ApJ, 753, 104
Mendez, A. J., Coil, A. L., Aird, J., et al. 2016, ApJ, 821, 55
Mullaney, J. R., Del-Moro, A., Aird, J., et al. 2015, ApJ, 808, 184
Netzer, H. 2015, ARA&A, 53, 365
Nousek, J. A., & Shue, D. R. 1989, ApJ, 342, 1207
Radburn-Smith, D. J., Lucey, J. R., Woudt, P. A., Kraan-Korteweg, R. C., & Watson, F. G. 2006, MNRAS, 369, 1131
Reyes, R., Zakamska, N. L., Strauss, M. A., et al. 2008, AJ, 136, 2373
Ricci, C., Bauer, F. E., Treister, E., et al. 2017, MNRAS, 468, 1273
Ricci, C., Ueda, Y., Koss, M. J., et al. 2015, ApJL, 815, L13
Risaliti, G. 2002, A&A, 386, 379
Sanders, D. B., Soifer, B. T., Elias, J. H., et al. 1988, ApJ, 325, 74
Schawinski, K., Thomas, D., Sarzi, M., et al. 2007, MNRAS, 382, 1415
Setti, G., & Woltjer, L. 1989, A&A, 224, L21
Stern, D. 2015, ApJ, 807, 129
Stern, D., Assef, R. J., Benford, D. J., et al. 2012, ApJ, 753, 30
Stern, D., Eisenhardt, P., Gorjian, V., et al. 2005, ApJ, 631, 163
Stern, D., Lansbury, G. B., Assef, R. J., et al. 2014, ApJ, 794, 102
Teng, S. H., Rigby, J. R., Stern, D., et al. 2015, ApJ, 814, 56
Treister, E., Natarajan, P., Sanders, D. B., et al. 2010, Sci, 328, 600
Treister, E., Urry, C. M., & Virani, S. 2009, ApJ, 696, 110
Ueda, Y., Akiyama, M., Hasinger, G., Miyaji, T., & Watson, M. G. 2014, ApJ, 786, 104
Urry, C. M., & Padovani, P. 1995, PASP, 107, 803
Vasudevan, R. V., Brandt, W. N., Mushotzky, R. F., et al. 2013, ApJ, 763, 111
Veilleux, S., & Osterbrock, D. E. 1987, ApJS, 63, 295
Vignali, C., Alexander, D. M., & Comastri, A. 2006, MNRAS, 373, 321
Vignali, C., Alexander, D. M., Gilli, R., & Pozzi, F. 2010, MNRAS, 404, 48
Wu, J., Brandt, W. N., Hall, P. B., et al. 2011, ApJ, 736, 28
Yang, G., Brandt, W. N., Luo, B., et al. 2016, ApJ, 831, 145
Yuan, F.-T., Takeuchi, T. T., Matsuoka, Y., et al. 2012, A&A, 548, A117
Zakamska, N. L., Strauss, M. A., Krolik, J. H., et al. 2003, AJ, 126, 2125
Zappacosta, L., Comastri, A., Civano, F., et al. 2017, ApJ, in press